Central Amygdala *Prepronociceptin*-Expressing Neurons Mediate Palatable Food Consumption and Reward

J. Andrew Hardaway,[1,2,3,*] Lindsay R. Halladay,[14,15] Christopher M. Mazzone,[1,2,6] Dipanwita Pati,[1,2] Daniel W. Bloodgood,[1,2,6] Michelle Kim,[1,2] Jennifer Jensen,[1,2] Jeffrey F. DiBerto,[1,2] Kristen M. Boyt,[1,2] Ami Shiddapur,[1,2] Ava Erfani,[1,2] Olivia J. Hon,[1,2,6] Sofia Neira,[1,2,6] Christina M. Stanhope,[1,2] Jonathan A. Sugam,[1,2] Michael P. Saddoris,[7] Greg Tipton,[1,2] Zoe McElligott,[1,2,3] Thomas C. Jhou,[13] Garret D. Stuber,[3,4] Michael R. Bruchas,[9,10,11,12] Cynthia M. Bulik,[3,5,8] Andrew Holmes,[14] and Thomas L. Kash[1,2,16,*]

[1]Bowles Center for Alcohol Studies, University of North Carolina at Chapel Hill School of Medicine, Chapel Hill, NC 27599, USA
[2]Department of Pharmacology, University of North Carolina at Chapel Hill School of Medicine, Chapel Hill, NC 27599, USA
[3]Department of Psychiatry, University of North Carolina at Chapel Hill School of Medicine, Chapel Hill, NC 27599, USA
[4]Department of Cell Biology and Physiology, University of North Carolina at Chapel Hill School of Medicine, Chapel Hill, NC 27599, USA
[5]Department of Nutrition, University of North Carolina at Chapel Hill, Chapel Hill, NC 27599, USA
[6]Neurobiology Curriculum, University of North Carolina at Chapel Hill, Chapel Hill, NC 27599, USA
[7]Department of Psychology and Neuroscience, University of Colorado, Boulder, Boulder, CO 80309, USA
[8]Department of Medical Epidemiology and Biostatistics, Karolinska Institutet, Stockholm, Sweden
[9]Division of Basic Research, Department of Anesthesiology, Washington University in St. Louis School of Medicine, St. Louis, MO 63110, USA
[10]Center for Neurobiology of Addiction, Pain, and Emotion, University of Washington, Seattle, WA 98195, USA
[11]Department of Anesthesiology and Pain Medicine, University of Washington, Seattle, WA 98195, USA
[12]Department of Pharmacology, University of Washington, Seattle, WA 98195, USA
[13]Department of Neuroscience, Medical University of South Carolina, Charleston, SC 29425, USA
[14]Laboratory of Behavioral and Genomic Neuroscience, National Institute on Alcohol Abuse and Alcoholism, NIH, Bethesda, MD, USA
[15]Department of Psychology, Santa Clara University, Santa Clara, CA 95053, USA
[16]Lead Contact
*Correspondence: hardawayja@gmail.com (J.A.H.), thomas_kash@med.unc.edu (T.L.K.)
https://doi.org/10.1016/j.neuron.2019.03.037

SUMMARY

Food palatability is one of many factors that drives food consumption, and the hedonic drive to feed is a key contributor to obesity and binge eating. In this study, we identified a population of prepronociceptin-expressing cells in the central amygdala (*Pnoc*^{CeA}) that are activated by palatable food consumption. Ablation or chemogenetic inhibition of these cells reduces palatable food consumption. Additionally, ablation of *Pnoc*^{CeA} cells reduces high-fat-diet-driven increases in bodyweight and adiposity. *Pnoc*^{CeA} neurons project to the ventral bed nucleus of the stria terminalis (vBNST), parabrachial nucleus (PBN), and nucleus of the solitary tract (NTS), and activation of cell bodies in the central amygdala (CeA) or axons in the vBNST, PBN, and NTS produces reward behavior but did not promote feeding of palatable food. These data suggest that the *Pnoc*^{CeA} network is necessary for promoting the reinforcing and rewarding properties of palatable food, but activation of this network itself is not sufficient to promote feeding.

INTRODUCTION

Feeding is a complex behavior regulated by central and peripheral signals. Alterations of these signals underlie behavioral pathologies of conditions like obesity and binge-eating disorder. One hypothesis to account for the excess in energy intake relative to energy expenditure that occurs acutely in binge-eating disorder and chronically in obesity is that humans often eat for hedonic, or rewarding, reasons rather than to maintain caloric homeostasis (Berthoud et al., 2011). Binge-eating disorder, in particular, is defined by the presence of recurrent binges or the uncontrolled consumption of an unusually large amount of food in a short amount of time.

Both animal and neuroimaging studies in humans have revealed that energy-dense palatable foods are capable of activating brain circuits in the amygdala and that the amygdala is activated in response to food-predictive cues or food consumption (O'Doherty et al., 2002; Small, 2012; Small et al., 2008). Testing the causal role of amygdala brain circuitry for feeding behavior in humans, however, is difficult. Among the many challenges is that the amygdala is composed of several interconnected regions with heterogeneous cell types expressing different neurotransmitters and neuropeptides. At present, it is unclear how changes in bulk activity measured in neuroimaging relate to the activity of individual neurons in the amygdala. Neural circuit level approaches attempt to untangle these complex

landscapes of heterogeneous cellular networks working in close three-dimensional proximity.

The central amygdala (CeA) is composed of GABAergic neurons that express neuropeptides or signaling molecules, such as corticotropin releasing factor, neuropeptide Y, somatostatin, neurotensin, enkephalin, dynorphin, nociceptin, and various kinases (Chieng et al., 2006; Gilpin et al., 2015; Moga and Gray, 1985; Neal et al., 1999). One class of neurons, expressing protein kinase C δ (PKCδ), are activated by aversive anorexigenic signals like cholecystokinin (CCK), lipopolysaccharide, or lithium chloride (Amano et al., 2012; Cai et al., 2014; Haubensak et al., 2010). Optogenetic activation of PKCδ neurons robustly suppresses food intake through the local release of gamma-aminobutyric acid (GABA) in the CeA (Cai et al., 2014). CeA PKCδ neurons receive excitatory glutamatergic inputs from anorexigenic calcitonin-gene-related peptide (CGRP) neurons in the parabrachial nucleus (PBN) (Campos et al., 2016, 2018; Carter et al., 2013, 2015), which receive glutamatergic inputs from both tyrosine hydroxylase (TH) and CCK cells located in the nucleus of the solitary tract (NTS) (D'Agostino et al., 2016; Roman et al., 2016). Taken together, this ascending network inhibits food consumption and is a critical mediator of negative valence, satiation, and conditioned taste aversion. Although anatomical description of output circuitry from the CeA is well known (Gray and Magnuson, 1987), a role for these pathways regulating hedonic food consumption has not yet been described.

Consumption of palatable foods is known to increase the expression of activity-dependent genes like Fos in the CeA (Park and Carr, 1998; Valdivia et al., 2014; Wu et al., 2014), but the encoding and functional role of neuronal networks in the CeA activated by foods associated with positive valence is unknown. In this study, we demonstrate that the CeA is robustly activated by palatable food consumption and that a subset of these activated CeA neurons express prepronociceptin, the precursor to the orexigenic opioid-like neuropeptide nociceptin. *Pnoc*^{CeA} neurons promote palatable food consumption specifically, are required for chronic high-fat-diet-induced obesity, and promote reward seeking through local connections in the CeA and axonal projections to the ventral bed nucleus of the stria terminalis (vBNST), PBN, and NTS.

RESULTS

Generation and Characterization of Pnoc-IRES-Cre Mouse

Nociceptin/orphanin FQ injection promotes feeding behavior, and nociceptin receptor antagonists can reduce palatable food consumption (Hardaway et al., 2016; Pomonis et al., 1996; Statnick et al., 2016). To capture the role of the endogenous nociceptin network, we inserted Cre recombinase into the endogenous mouse prepronociceptin (*Pnoc*) locus (*Pnoc*$^{IRES\text{-}Cre}$; Figure 1A). Following a cross of these animals to the *Ai9* reporter strain (*Pnoc*$^{IRES\text{-}Cre}$; *Ai9*:*Rosa26*-loxp-STOP-loxp-TdTomato), we observed a large number of labeled cells and fibers throughout the brain (Figure 1B), concentrating in areas known for enrichment of *Pnoc* mRNA, such as the lateral septum (LS) (Figures 1B and S1A), BNST (Figure S1A), multiple hypothalamic nuclei (Figure S1A), and the CeA (Ikeda et al., 1998). To verify the fidelity of Cre expression in this mouse line, we performed dual fluorescence *in situ* hybridization for *Cre* and *Pnoc* in the CeA of *Pnoc*$^{IRES\text{-}Cre}$ mice (Figures 1C–1E). We observed detectable *Cre* expression in >50% of the *Pnoc*-expressing cells, and >90% of the *Cre*-expressing cells also expressed *Pnoc* (Figure 1F). Thus, we determined that the *Pnoc*$^{IRES\text{-}Cre}$ mouse is a robust, high-fidelity strain by which to gain genetic access to nociceptin networks in the CeA.

To describe the landscape of *Pnoc*-expressing cells in the CeA and throughout the brain, we used IDISCO+ in *Pnoc*$^{IRES\text{-}Cre}$; *Ai9* mice, light sheet microscopy, and the ClearMap analysis pipeline (Renier et al., 2014, 2016; Figure 1G). After ClearMap, we extracted digital positions of segmented cells in the CeA and plotted their density along the A-P axis (Figure 1H). We observed *Pnoc* cells along the entire length of the anterior- posterior (A-P) axis of the CeA but a greater number between −1.1 and −1.7 mm posterior of bregma. We observed *Pnoc*-expressing cells in both the lateral central nucleus (CeL) and medial central nucleus (CeM) of the amygdala. We then used *ex vivo* slice patch-clamp electrophysiology in *Pnoc*$^{IRES\text{-}Cre}$; *Rosa26*-loxp-STOP-loxp-L10-GFP (*Pnoc*-GFP) mice to characterize basal neuronal properties of *Pnoc*^{CeA} neurons, which were consistent with low-threshold bursting population of neurons that also show hyperpolarization-activated inward current in the CeA as previously reported (Figures 1I–1M). Consistent with these IDISCO and electrophysiological data, we observed a high number of cells expressing *Pnoc* in this range of the CeA, as revealed by confocal imaging of *Pnoc*$^{IRES\text{-}Cre}$; *Ai9* mice and fluorescence *in situ* hybridization of *Pnoc* mRNA (Figures S2A–S2Gi). Additionally, ClearMap revealed a complex array of *Pnoc*-expressing cells in multiple brain regions consistent with our observations in fixed slices from *Pnoc*$^{IRES\text{-}Cre}$; *Ai9* mice (Figure S1A; Table S1).

To gain a better understanding of the overlap of the *Pnoc*^{CeA} network relative to other cellular networks in the CeA, we performed dual fluorescence *in situ* hybridization with *Pnoc* and *Crh*, *Nts*, *Calcr*, *Tac2*, *Prkcd*, *Sst*, and *Htr2a* (Figures S2A–S2G). Consistent with our IDISCO experiments in *Pnoc*$^{IRES\text{-}Cre}$; *Ai9* reporter mice and imaging of fixed confocal slices, we observed a large population of *Pnoc*-mRNA-expressing cells in the CeA. In counts of both the CeL and the CeM, *Pnoc* cells had weak overlapping expression with *Crh* (5.4%), *Nts* (12.2%), *Calcr* (6.8%), *Tac2* (12.6%), *Prkcd* (18.6%), *Sst* (19.5%), and *Htr2a* (14.7%). Across all of these markers, we observed very robust expression in the CeA except for *Htr2a* (Figure S2F), which had very weak overall expression except for the ventral CeM and capsular central nucleus (CeC). Additionally, we determined the overlap of *Pnoc*-labeled cells with protein kinase C delta (PKCδ) and somatostatin (SST) using immunohistochemistry in *Pnoc*$^{IRES\text{-}Cre}$; *Ai9* mice in the lateral CeA (Figures S2H and S2I). In the CeL, we found very little (8.7%) overlap of *Pnoc* with PKCδ (Figure S2H). *Pnoc* cells often expressed SST (34.3%), but we observed an equal number of *Pnoc*-only- and SST-only-expressing cells (Figure S2I). Therefore, we determined that *Pnoc*^{CeA} cells are a novel CeA cell population that has detectable but weak overlap with a number of CeA cell types, including SST neurons.

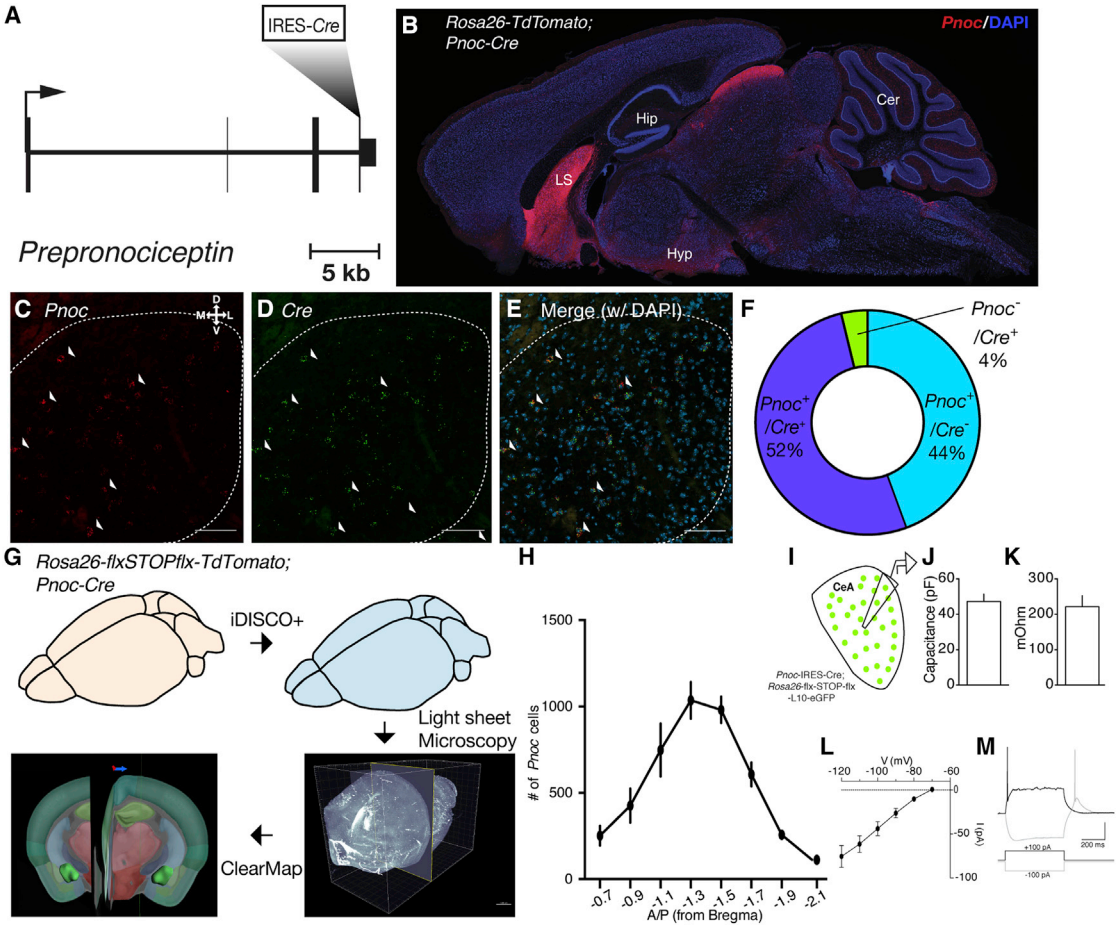

Figure 1. Anatomical Characterization of the Central Amygdala Prepronociceptin System

(A) Schematic of targeting of IRES-Cre cassette into the endogenous Prepronociceptin gene.

(B) Sagittal section of *Pnoc*$^{IRES\text{-}Cre}$; *Rosa26*-flx-stop-flx-TdTomato (*Ai9*) mice.

(C–E) Example images of *Pnoc* (C; red), *Cre* (D; green), and merge (E) mRNA expression in the CeA. Scale bars represent 50 μM.

(F) Quantification of *Pnoc*, *Cre*, and double-positive cell counts across all CeA images.

(G) Schematic of tissue clearing, IDISCO+, light sheet microscopy, and ClearMap workflow in *Pnoc*$^{IRES\text{-}Cre}$; *Ai9* mice.

(H) Quantification of *Pnoc*+ cells across the A-P axis following extraction of segmented *Pnoc* cell coordinates after ClearMap.

(I) Schematic of *ex vivo* recordings of *Pnoc*-GFP reporter mice.

(J) Average membrane capacitance (C_m) of *Pnoc* neurons.

(K) Average membrane resistance (R_m) of *Pnoc* neurons.

(L) Hyperpolarization-activated inward (Ih) currents in *Pnoc* neurons.

(M) Example low-threshold bursting in response to depolarizing current step.

For (J) and (K), n = 13 cells from 3 mice.

Pnoc^{CeA} Neurons Are Activated by the Consumption of Highly Palatable, Calorically Dense Food

To determine the role of the endogenous amygdalar nociceptin-expressing neuronal network in feeding, we exposed *Pnoc*$^{IRES\text{-}Cre}$; *Ai9* mice to either intermittent (1-h) or continuous (24-h) palatable high-fat diet (HFD) and assessed the expression of the immediate early gene Fos. Intermittent access to HFD is a form of palatability-induced hyperphagia and a face valid preclinical model of binge eating and is known for producing robust, time-locked food consumption that mostly occurs within the first 10 min of food exposure (Hardaway et al., 2016). We identified a significant increase in Fos+/*Pnoc*+ cells in the CeA of animals exposed to intermittent HFD relative to continuous HFD or *ad libitum* chow-only controls (Figures 2A–2D). Therefore, CeA *Pnoc* cells (*Pnoc*^{CeA}) are activated following intermittent access-induced HFD consumption. The basolateral amygdala (BLA) is a neighboring amygdala subdivision that has been shown to express higher levels of Fos following fasting and refeeding (Wu et al., 2014). Histological analysis revealed detectable but scattered *Pnoc*-expressing cells in the BLA, and although we observed an increase in the total number Fos+ cells in intermittent HFD animals (Figures S1B–S1E), we did not observe an increase in the number of Fos+/*Pnoc*+ cells (Figure S1F).

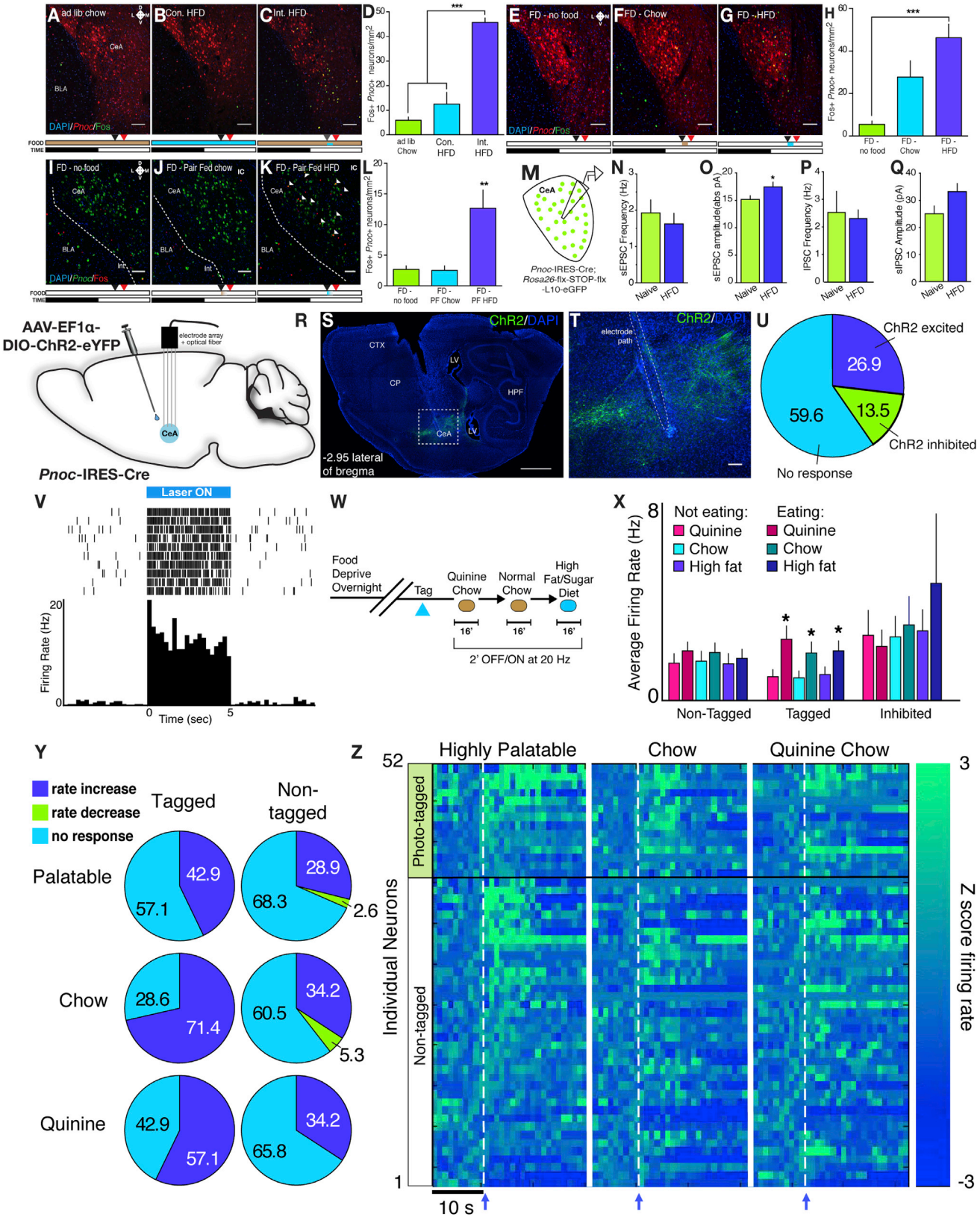

(legend on next page)

We observed that *Pnoc*^{CeA} neurons are activated following intermittent HFD consumption relative to chow-only or continuous HFD (Figures 2A–2D). We hypothesized that the lack of Fos expression in chow-only and continuous HFD groups may be mediated by a lack of recent food intake. In a separate group of *Pnoc*$^{IRES\text{-}Cre}$; *Ai9* mice, we food-deprived animals overnight and exposed them to no food, *ad libitum* chow, or *ad libitum* HFD. We observed a significant increase in Fos+/*Pnoc*+ cells in HFD animals relative to no food controls (Figures 2E–2H), and although we observed an overall increase in Fos+/*Pnoc*+ cells in chow-refed animals, this did not reach statistical significance relative to no food controls (Figure 2H). Importantly, across all three groups, we observed a significant linear relationship between the amount of either total Fos cells or Fos+/*Pnoc*+ cells and the total caloric intake (Figures S1G and S1H) using this *ad libitum* design. To directly control the level of food intake, we food deprived *Pnoc*-GFP mice and exposed them to either no food or an isocaloric amount of either chow or HFD. We used a caloric amount that was less than half of what would be consumed during an intermittent HFD session or a food deprivation-chow refeed paradigm that we hypothesized would not produce satiation. Using this pair-fed matched design, we observed a significant increase in Fos+/*Pnoc*+ cells only in the HFD condition relative to the no food and chow-only controls (Figures 2I–2L). This suggests that *Pnoc*^{CeA} cells are activated in a calorically scalar manner by food consumption in general and by palatable food in particular and that the activation of *Pnoc*^{CeA} cells occurs putatively independent of satiation.

Neurons in the CeA exhibit plasticity in response to stimuli of positive and negative valence and are capable of generating state-dependent appetitive or avoidance behavior (Fadok et al., 2018; Li et al., 2013). We used *ex vivo* slice patch-clamp electrophysiology in *Pnoc*-GFP mice to measure spontaneous inhibitory and excitatory postsynaptic currents (sIPSCs and sEPSCs) in naive animals or animals exposed to intermittent HFD for 1 h. Comparing naive animals to those with intermittent access to HFD, we observed no changes in sIPSC and sEPSC frequency in *Pnoc*^{CeA} neurons in HFD-exposed animals (Figures 2N and 2P). However, we observed a significant increase in sEPSC, but not sIPSC, amplitude in *Pnoc*^{CeA} neurons from animals that consumed HFD (Figures 2O and 2Q). These data suggest that a single bout of HFD exposure can promote changes in excitatory synaptic function in these neurons, supporting their potential role in feeding-related behavior.

To gain a fuller picture of the dynamic recruitment of *Pnoc*^{CeA} neurons during food consumption, and in response to food associated with negative and positive valence, we measured changes in the firing rates of *Pnoc*^{CeA} neurons *in vivo* using an optical tagging electrophysiological approach. We virally expressed channelrhodopsin-2 (ChR2) in the CeA of *Pnoc*$^{IRES\text{-}Cre}$ animals and simultaneously implanted animals unilaterally with an optical fiber or electrode array (Figures 2R–2T). After recovery from surgery, we identified 14 putative *Pnoc*^{CeA} neurons (tagged) that responded with a latency of <5 ms during 10× 5′ trains of blue light and 35 non-*Pnoc*^{CeA} neurons using this approach (Figures 2U and 2V). Among the non-*Pnoc* neurons, we identified 7 units that displayed time-locked inhibition and 28 single units

Figure 2. *Pnoc*^{CeA} Neurons Are Activated during Feeding

(A–D) Example images and quantification of Fos immunoreactivity in the CeA from *Ai9* (TdTomato) mice being fed under *ad lib* chow conditions (A), continuous (B), or intermittent (C) access to high-fat diet (Int. HFD). The timeline of the experiment for each group is depicted below the image where beige denotes chow, blue denotes HFD, black arrow denotes the start of the experiment, and red denotes the time of perfusion (100 min following start).

(D) Quantification of Fos from different feeding conditions (n = 3/group; one-way ANOVA with Tukey's multiple comparisons test $F_{(2,6)} = 49.17$; $p < 0.001$).

(E–H) Example images and quantification of Fos immunoreactivity in the CeA from reporter mice that were food deprived overnight and then provided with either no food (E), *ad lib* chow (F), or *ad lib* HFD (G). Timeline of the experiment is below. n = 4/group.

(H) Quantification of Fos from refeeding experiment (n = 4/group; one-way ANOVA with Tukey's multiple comparisons test $F_{(2,9)} = 12.20$; $p = 0.0027$).

(I–L) Example images and quantification of Fos immunoreactivity in the CeA from *Pnoc*-GFP mice that were food deprived overnight and then provided with no food (I) or a nonsatiating isocaloric amount of either chow (J) or HFD (K). Arrowheads denote colabeled Fos+/*Pnoc*+ cells. Timeline of experiment is identical to (E)–(H). n = 5/group.

(L) Quantification of Fos from refeeding experiment (n = 5/group; one-way ANOVA with Tukey's multiple comparisons test $F_{(2,12)} = 10.20$; $p = 0.0026$). Scale bars represent 50 μM.

(M) Schematic of electrophysiological recordings from *Pnoc*-GFP mice.

(N–Q) Synaptic transmission measurements from *Pnoc*^{CeA} neurons in either naive or HFD-fed *Pnoc*$^{IRES\text{-}Cre}$; Rosa26-flx-stop-flx-L10-GFP mice.

(N) sEPSC frequency (n = 14 cells from 5 mice for naive control group and n = 29 cells from 7 mice for HFD group; unpaired Student's t test; $p = 0.5232$).

(O) sEPSC amplitude (n = 14 cells from 5 mice for naive control group and n = 29 cells from 7 mice for HFD group; unpaired Student's t test; $p = 0.0456$).

(P) sIPSC frequency (n = 9 cells from 5 mice for naive control group and n = 27 cells from 7 mice for HFD group; unpaired Student's t test; $p = 0.7966$).

(Q) sIPSC amplitude (n = 9 cells from 5 mice for naive control group and n = 27 cells from 7 mice for HFD group; unpaired Student's t test; $p = 0.0583$).

(R) Schematic of AAV-ChR2 injection and unilateral multielectrode array placement in *Pnoc*$^{IRES\text{-}Cre}$ mice.

(S) Example sagittal image showing electrode path and viral transduction. CP, caudate putamen; CTX, cortex; HPF, hippocampal formation; LV, lateral ventricle; scale bars represent 1 mm.

(T) Enlarged view of (S) showing electrode path and damage from electrolytic lesions.

(U) Distribution of neurons according to responses during 10 5′ blue light pulses tagging session.

(V) Raster plot and spike histogram of an example optically tagged neuron.

(W) Schematic of three food exposures following optical tagging of *Pnoc*^{CeA} neurons.

(X) Raw average firing rates across non-eating and eating epochs from non-tagged, tagged, and inhibited neuron populations during laser off blocks. n = 28 non-tagged neurons, fourteen tagged neurons, and seven inhibited neurons. Data were analyzed using a 3 × 2 repeated-measures ANOVA comparing the effect of eating across each food type.

(Y) Pie charts showing percent of neurons that responded to each food type in the non-tagged and tagged neuron groups using *Z* score changes > 2.56.

(Z) Heatmaps of individual neuron responses to food consumption across three food types. Arrow and dashed line indicates the onset of chewing.

(non-tagged) that showed no change (Figure 2U). These animals were food deprived overnight and then provided short-term access to quinine-adulterated chow, vehicle (water)-adulterated chow, and then HFD (Figure 2W). We then analyzed neural activity during epochs of food consumption. In tagged neurons, but not non-tagged and inhibited neurons, we observed a significant increase in the average firing rate during consumption of each food type (Figure 2X). Analysis of single unit *Z* scores changes during consumption revealed that a significant and higher fraction of tagged *Pnoc*^{CeA} neurons are activated during consumption of quinine-adulterated chow, vehicle (water)-adulterated chow, or HFD than non-tagged neurons (Figures 2Y and 2Z). Consistent with our Fos data, these data demonstrate that *Pnoc*^{CeA} neurons are dynamically recruited during food consumption across a spectrum of taste valence.

Pnoc^{CeA} Cells Promote HFD Consumption and HFD-Induced Obesity

To probe the functional role of *Pnoc*^{CeA} cells, we injected *Pnoc*-GFP animals with an adeno-associated virus (AAV) expressing a Cre-dependent proteolytic caspase complex that triggers apoptosis (Yang et al., 2013; Figure 3A). *Post hoc* examination of the number of GFP+ cells in the CeA of mice injected with caspase virus revealed a ~50% reduction in the number of *Pnoc*^{CeA} cells normalized to the adjacent lateral hypothalamus (LH) relative to control virus-injected animals (Figures 3B–3D). To assess the functional contribution of *Pnoc*^{CeA} cells to acute food intake, body composition, and metabolism, we injected *Pnoc*-GFP animals with caspase or control virus and allowed them to recover for 4 weeks. We then measured their body composition using MRI and then transferred the animals to individual comprehensive lab animal monitoring system (CLAMS) cages and measured activity, food intake, water intake, and calorimetry. Following 7 days of acclimation to CLAMS cages with *ad libitum* chow, we provided each animal with 1 h of intermittent access to HFD (along with *ad libitum* chow) over 4 days (5 sessions) and continuous HFD access (no chow) for 3 days (Figure 3E). Water was always available *ad libitum*. In this way, we assessed the contribution of *Pnoc*^{CeA} cells on multiple aspects of consumption and physiology. At baseline (T1), there was no impact on any of the measurements performed (Figures S3A–S3D); however, following exposure to HFD, we found a significant reduction in the percent change in bodyweight (Figure 3F) and fat mass (Figure 3G) but no other properties (Figures S3E–S3V and S3X). This appeared to be driven by reduced HFD consumption and a significant reduction in the respiratory exchange ratio (Figures 3H–3J) in caspase mice. Consistent with previous observations (Jais et al., 2016), we observed an overall decrease and loss of diurnal rhythms in respiratory exchange ratio (RER) values in both groups during continuous HFD (Figure S3W). A separate analysis of core body temperatures prior to and after 3 days of HFD access revealed that caspase-injected animals show a reduction in core body temperature following 3 days of HFD access, regardless of the light cycle (Figure 3K). To assess whether ablation of these neurons regulated homeostatic feeding, we assessed chow intake following overnight food deprivation and observed no significant difference in 3-h chow intake (Figure 3L). Additionally, using calorimetry, we observed no differences in respiratory exchange during a 7-h fast (Figure S3Y). These data suggest that *Pnoc*^{CeA} neurons have minimal effects on basal metabolism and homeostatic feeding, whereas they play a key role in the consumption of HFD.

We wanted to determine whether our previous observations extended to noncaloric tastants. Thus, in a separate cohort of animals, we tested the impact of *Pnoc*^{CeA} neuron ablation on 24-h two bottle choice preference for both palatable and unpalatable liquid tastants (Kovacs et al., 2005; Figures 3M and 3N; validation in Figure S3Z). Loss of *Pnoc*^{CeA} neurons resulted in enhanced aversion to a high concentration of quinine, a noncaloric bitter tastant, and a significant reduction in preference for low and high concentrations of saccharin, a noncaloric sweet tastant (Figure 3N). We did not observe a significant reduction in preference for 1% sucrose. Together, these studies demonstrated that ablation of *Pnoc*^{CeA} cells reduced palatable food consumption and palatable tastant preference and altered the way in which acute HFD impacts physiology (bodyweight, fat mass, respiratory exchange, and core body temperature).

Long-term access to highly palatable, calorically dense food is a face valid model of obesity, and animals will develop symptoms that resemble type II diabetes, like glucose intolerance and insulin or leptin resistance (Hariri and Thibault, 2010). In a separate cohort of caspase animals, we addressed the impact of *Pnoc*^{CeA} ablation on bodyweight in animals exposed to chow for 5 weeks, 1 week of intermittent HFD access, and 9 weeks of continuous HFD access (Figure 3O; validation in Figure S3AA). Using this design, we matched the *ad libitum* chow access and intermittent access HFD periods to our previous study but expanded the HFD access period from 3 days to 9 weeks. Consistent with what we observed following short-term access to HFD, we observed a significant reduction in bodyweight in caspase animals after chronic HFD access (Figure 3O). These data demonstrate that *Pnoc*^{CeA} cells are required for chronic HFD effects on bodyweight.

Inhibition of Pnoc^{CeA} Cells Reduces Palatable Food Consumption

To determine whether activation of *Pnoc*^{CeA} cells is required for the consumption of palatable food, we injected an AAV that expresses the inhibitory Gi-coupled designer receptor exclusively activated by designer drug (DREADD) hM4D-mCherry in a Cre-dependent fashion into the CeA (Armbruster et al., 2007; Figure 4A). Histological validation of these animals revealed specific mCherry expression in the CeA similar to what we observed in *Pnoc*$^{IRES\text{-}Cre}$; *Ai9* mice (Figure 4B). To measure the function of hM4D in *Pnoc*^{CeA} cells, we used *ex vivo* slice electrophysiology to assay hM4D effects on measures of neuronal resting membrane potential in current clamp mode. We found that bath application of clozapine-N-oxide (CNO) produces a >5 mV hyperpolarization in *Pnoc*^{CeA} cells and leads to increased rheobase and reduced current-induced action potentials (Figure 4C). To determine the impact of *Pnoc*^{CeA} chemogenetic inhibition on palatable food consumption, we injected CNO 30 min prior to exposure to HFD in the mouse's home cage. We observed that inhibition of *Pnoc*^{CeA} neurons reduced 1-h HFD consumption on their first exposure to HFD (Figure 4D). On subsequent sessions with access to HFD, the CNO-mediated

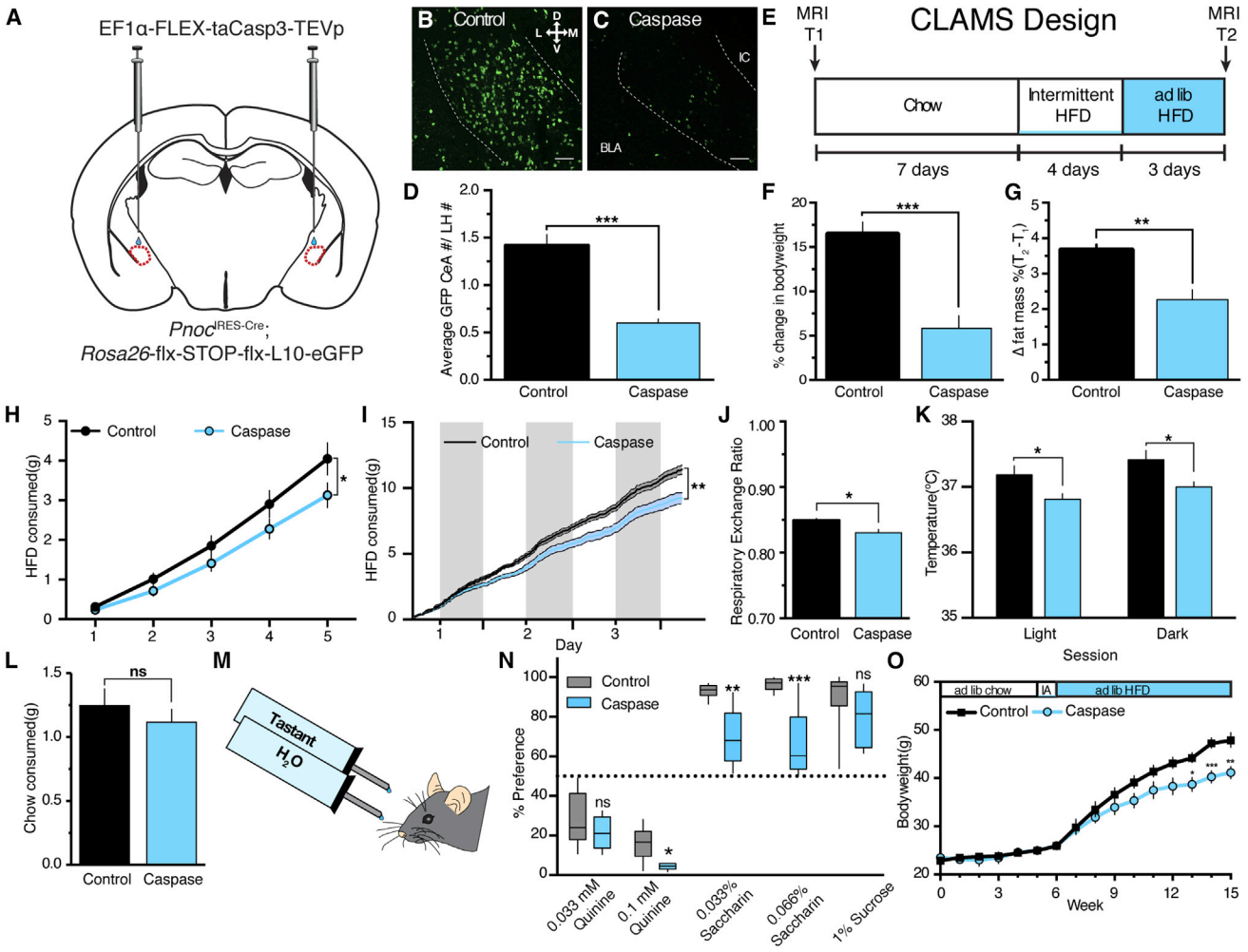

Figure 3. Ablation of *Pnoc*^{CeA} Neurons Reduces HFD Consumption and Promotes Resistance to HFD-Induced Obesity

(A) Schematic of CeA injection of viral Cre-dependent caspase complex in *Pnoc*-GFP reporter mice.

(B–D) Example images and quantification of *Pnoc*^{CeA} density in control (B) and caspase (C)-expressing animals. Scale bars represent 50 μM.

(D) Data are presented normalized to counts in the uninjected and neighboring zona incerta or lateral hypothalamus from the same section. See STAR Methods for details (n = 8 caspase and 7 control mice, unpaired Student's t test; $p < 0.0001$).

(E) Timeline of experiment in comprehensive lab animal monitoring system (CLAMS) cages. See Figure S3 for full dataset.

(F) Percent change in bodyweight from T1 to T2 in CLAMS experiment (n = 8 caspase and 7 control mice; unpaired Student's t test; $p < 0.0001$).

(G) Percent change in fat mass from T1 to T2 in CLAMS experiment (n = 8 caspase and 7 control mice; unpaired Student's t test; $p < 0.01$). See Figure S3 for full dataset.

(H) Cumulative binge HFD intake during 4 days of intermittent access and 1st hour of access during continuous HFD period (5 intermittent access HFD sessions; n = 8 caspase and 7 control mice; two-way repeated-measures ANOVA with Sidak's multiple comparisons test; session × group interaction; $F_{(4,52)} = 2.928$; $p = 0.0294$).

(I) Cumulative HFD intake for continuous HFD period. Shaded columns indicate lights off (n = 8 caspase and 7 control mice; two-way repeated-measures ANOVA with Sidak's multiple comparisons test; time × group interaction; $F_{(137,1,781)} = 11.42$; $p < 0.0001$).

(J) Average respiratory exchange during the continuous HFD period (n = 8 caspase and 7 control mice; unpaired Student's t test; $p = 0.0109$).

(K) Core body temperatures after 3 days of continuous HFD access in the home cage (n = 8 caspase and 7 control mice; two-way ANOVA with Sidak's multiple comparisons test; group effect; $F_{(1,24)} = 13.12$; $p = 0.0014$).

(L) Chow consumption following overnight food deprivation in control and caspase mice (n = 8 caspase and 7 control mice; unpaired Student's t test; $p = 0.4379$).

(M) 24-h two-bottle choice design.

(N) 2-bottle choice preference for quinine, saccharin, and sucrose (n = 5 caspase and 8 control mice; unpaired Student's t test for each tastant; $p = 0.6190$ [0.033 mM quinine]; $p = 0.01$ [0.1 mM quinine]; $p = 0.001$ [0.033% saccharin]; $p = 0.0005$ [0.066% saccharin]; $p = 0.2591$[1% sucrose]). For all experiments, $^{*}p < 0.05$, $^{**}p < 0.01$, and $^{***}p < 0.001$.

(O) Average weekly bodyweights of a separate caspase and control cohort after 5 weeks of chow access, 1 week of intermittent HFD access, and 9 weeks of *ad libitum* HFD access. See Figure S2R for validation of this cohort (n = 7 caspase and 6 control mice; two-way repeated-measures ANOVA with Sidak's multiple comparisons test; time × group interaction; $F_{(15,165)} = 5.672$; $p < 0.0001$).

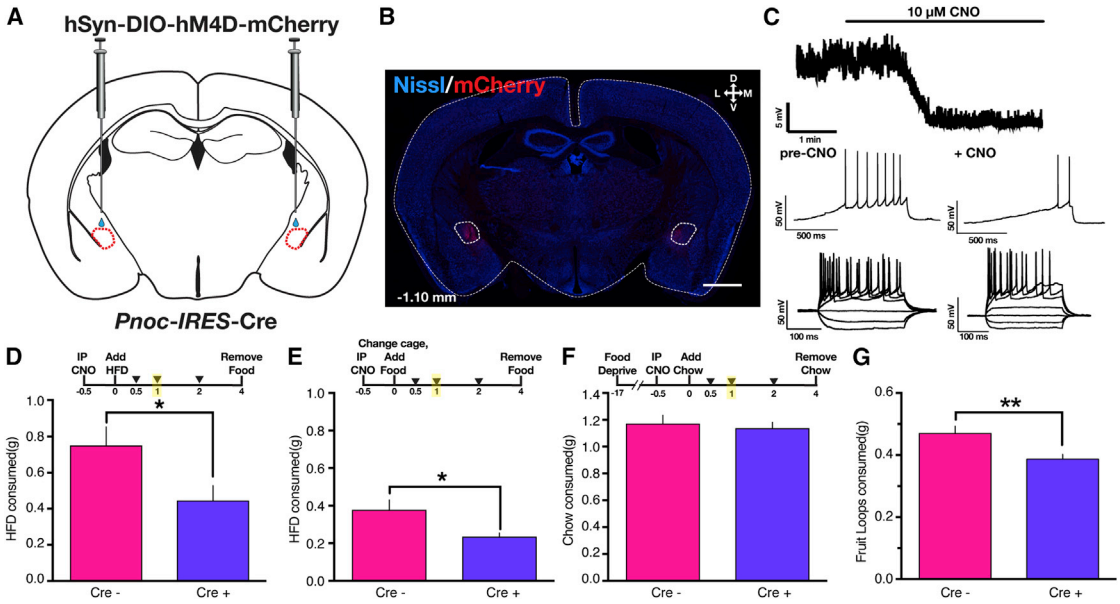

Figure 4. Chemogenetic Inhibition of *Pnoc*^{CeA} Neurons Reduces Palatable, Calorically Dense Food Intake

(A) Schematic of CeA injection of viral Cre-dependent hM4D-mCherry receptor in *Pnoc*$^{IRES\text{-}Cre}$ mice.

(B) Representative coronal section showing CeA-specific mCherry expression. Scale bar represents 1,000 µM.

(C) *Ex vivo* slice electrophysiological validation of hM4D function. Top: representative cell response to CNO bath application in current clamp mode is shown. Middle: representative cell response in current clamp mode to gradually increasing depolarizing current injection (rheobase) prior to and after CNO bath application is shown. Bottom: representative cell response in current clamp mode to increasing current steps is shown.

(D) 1-h HFD consumption in home cage during first exposure to HFD following 3 mg/kg intraperitoneal (IP) CNO injection 30 min before. p = 0.0258. Timeline of experiment depicted above where numbers indicate hours is shown. Bar graphs are from 1 h (highlighted time point).

(E) Later exposure to HFD in combination with cage bedding change. p = 0.0310.

(F) 1-h chow consumption following food deprivation and IP CNO. p = 0.7356.

(G) Fruit loop consumption during post-test home cage portion of novelty-induced suppression of feeding assay. p = 0.0089.

For (D)–(G), data were analyzed using an unpaired Student's t test, where *p < 0.05 and ** p <0.01. For all panels, n = 10 Cre+ and 11 Cre− animals.

suppression of HFD intake was lost (Figure S4A). These data are consistent with a role for novelty or stress in the way in which *Pnoc*^{CeA} neurons modulate palatable food intake. Stress is a known modulator of food intake and engages nociceptin signaling (Ciccocioppo et al., 2003), and we hypothesized that *Pnoc*^{CeA} neuronal modulation of food intake might interact with a stressor, such as a home cage bedding change. 30 minutes after injection with CNO, we simultaneously changed the mouse home cage and provided them access to HFD. We observed an overall decrease in both Cre+ and Cre− groups and a significant decrease in HFD consumption in hM4D-expressing animals relative to controls under these stress-induced conditions (Figure 4E). Finally, to probe how manipulation of these neurons can impact homeostatic feeding, we tested the effects of CNO on chow consumption following an overnight food deprivation or under *ad libitum* chow conditions. We observed no differences in chow intake in either of these paradigms following CNO (Figures 4F and S4B).

Anxiety and stress are potent suppressors of food intake (Hardaway et al., 2015), so we tested the impact of *Pnoc*^{CeA} chemogenetic inhibition on anxiety-like behavior as measured by the novelty-induced suppression of feeding, open field, elevated plus maze, elevated zero maze, and light-dark box conflict assays. In the novelty-induced suppression of feeding assay, we found that inhibition of *Pnoc*^{CeA} cells significantly increased the latency to feed (Figure S4C) and, consistent with our HFD observations, significantly decreased the consumption of fruit loops in the home cage post-test (Figure 4G). In the elevated plus maze, we observed that chemogenetic inhibition of *Pnoc*^{CeA} cells increased the mouse's average velocity and open arm time, but not the probability of an open arm entry (Figures S4D–S4F). In the light-dark box, we observed no significant differences in the time spent in the light zone (Figure S4G). Consistent with our findings in the elevated plus maze, we observed a significant increase in mouse velocity in the elevated zero maze (Figure S4H). We observed a significant increase in the distance traveled during exploration of an open field but no differences in center time in hM4D-expressing animals relative to controls (Figures S4I and S4J). These data are consistent with a role for *Pnoc*^{CeA} neurons in regulating locomotor responses to novel behavioral arenas and that inhibition of *Pnoc*^{CeA} neurons does not produce anxiety-like behavior.

In a separate cohort of mice, we tested the impact of chemogenetic inhibition of *Pnoc*^{CeA} neurons on water intake under *ad libitum* and 24-h water-deprived conditions. We observed no significant change in fluid intake (Figures S4K and S4L). Using water-deprived conditions, we tested the role of acute chemogenetic inhibition of *Pnoc*^{CeA} neurons on aversive tastant intake and preference in a 2-bottle choice paradigm. However, we observed no significant difference in quinine intake when we

acutely inhibit *Pnoc*^{CeA} neurons in this paradigm (Figure S4M). Lastly, to address whether *Pnoc*^{CeA} neurons are contributing to novel food intake versus palatable food intake, we assessed intake of a palatable tastant in combination with chemogenetic inhibition under conditions of novelty and familiarity (Figure S4N). To more closely match our previous experiment using high-fat diet, animals were not water deprived for these experiments. We observed no significant difference in Kool-Aid intake with inhibition of *Pnoc*^{CeA} neurons, regardless of whether the Kool-Aid was novel or familiar.

Pnoc^{CeA} Neurons Send Efferents to the BNST and Hindbrain

The CeA is the primary output nucleus of the amygdala, so we hypothesized that *Pnoc*^{CeA} neurons would send efferents to targets outside of the CeA. We injected *Pnoc*$^{IRES\text{-}Cre}$ animals with an AAV expressing the Cre-dependent anterograde tracer Synaptophysin-mCherry in the CeA (Figure 5A). These studies revealed a dense projection to the NTS, PBN, and vBNST (Figures 5B–5D). In the PBN, we observed dense mCherry expression in both the medial and lateral portions (Figures 5C, S4O, and S4P). Immunohistochemical co-stains for calcitonin-related gene peptide (CGRP) and tyrosine hydroxylase reveal *Pnoc*^{CeA} fibers in close apposition to CGRP+ (Figure S4Q), but not TH+, cell bodies (Figure S4O). In the NTS, we observed mCherry expression throughout the anterior-posterior portions of the NTS, including the dorsal motor vagal nucleus area postrema that did not extend beyond the caudal-most portion of the solitary nucleus and the pyramidal decussation (Figure 5B). In the BNST, we observed mCherry fluorescence in the anterior portions of the BNST, particularly the ventral BNST. Finally, we observed more sparse fibers in the ventral periaqueductal gray (Figure S4Q), substantia innominata (Figure S4R), hypothalamus (Figure S4S), paraventricular nucleus of the thalamus (Figure S4T), and reticular formation (Figure S4U). In these tracing experiments, we observed labeling of *Pnoc*-expressing cells in the basolateral portions of the amygdala (Figure S4V). To confirm the specificity of target tracing of *Pnoc*^{CeA} neurons, we injected animals with AAV-EF1α-DIO-Synaptophysin-mCherry biased more laterally in the BLA (Figure S4V). In the *Pnoc*^{BLA} tracing experiments, we observed reduced mCherry expression in the PBN, NTS, or vBNST (Figures S4W–S4Y), but we observed dense mCherry arborizations within the BLA (Figure S4V). Additionally, injections of the retrograde tracer cholera toxin subunit B (CTB) subunit in the NTS or PBN, but not BNST, revealed no labeled cells in the BLA (see below). These data demonstrate that *Pnoc*^{CeA} cells send axon terminals to the vBNST, PBN, and NTS.

Pnoc^{CeA} Hindbrain-Projecting Neurons Are Activated following HFD Consumption

To characterize the relevance of vBNST, PBN, or NTS-projecting *Pnoc*^{CeA} cells, we performed a multiplexed experiment using *Pnoc*-GFP animals injected with Alexa-Fluor-555-conjugated CTB in the BNST, PBN, or NTS combined with immunohistochemical detection of Fos following no exposure or 1-h access to HFD. Following BNST CTB injections, we observed robust CTB labeling of CeA cells in the medial and lateral portions and fibers in the interwoven stria terminalis (Figures 5Eiii and 5Eiv) that labeled 10%–15% of the total *Pnoc*^{CeA} cells (Figure 5H). For PBN CTB injections, we observed CTB labeling of cells primarily within the lateral CeA that labeled 10%–15% of the total *Pnoc*^{CeA} cells (Figure 5H). CTB injections into the NTS revealed CTB labeling primarily in the medial CeA of *Pnoc*-GFP animals that labeled 20%–30% of *Pnoc*^{CeA} cells (Figure 5H). In a separate analysis of all animals injected within a brain region and regardless of HFD consumption, a one-way ANOVA revealed significantly more NTS-projecting *Pnoc*^{CeA} cells than BNST or PBN (Figure S4Z). To determine the activity of these projecting cells, we compared Fos colabeling with CTB and *Pnoc* between animals with no HFD or intermittent 1-h access to HFD. These studies confirmed our previous observations that *Pnoc* cells are activated following HFD consumption across all three sets of CTB injections (Figure 5I). We observed a significant increase in Fos-labeled CTB cells in animals with injections in all three brains regions (Figure 5J); however, we only observed a significant increase in Fos-labeled *Pnoc*^{CeA} cells that project to the PBN or NTS and not the BNST (Figure 5K). These data demonstrate that PBN or NTS-projecting *Pnoc*^{CeA} cells, specifically, are activated following HFD consumption and that the *Pnoc*$^{CeA\text{-}PBN}$ and *Pnoc*$^{CeA\text{-}NTS}$ pathways may functionally contribute to HFD consumption.

Optogenetic Activation of Pnoc Neurons and Outputs to the vBNST, PBN, and NTS Promote Reward-like Behavior, but Not Food Consumption

Based on our anatomical and functional data of *Pnoc*^{CeA} cells, we hypothesized that *Pnoc*^{CeA} neuron activation might, through a local or output mechanism, drive positive valence and palatable food consumption. To assess whether *Pnoc*^{CeA} neurons make functional connections in the areas we observed significant innervation, we injected an AAV encoding a Cre-dependent channelrhodopsin (ChR2) and used whole-cell patch-clamp electrophysiology to characterize these efferents. In the CeA, we recorded from ChR2-expressing cells, where we observed blue-light-evoked action potentials in current clamp mode (Figures S5A and S5B). In the CeA, vBNST, PBN, and NTS, we recorded from cells in areas showing ChR2 expression using a paired pulse protocol (Figures 6A, 6G, 6M, and 6S) and observed blue-light evoked induced postsynaptic currents (iPSCs). These data demonstrate that *Pnoc*^{CeA} cells make functional inhibitory synapses within the CeA and to the vBNST, PBN, and NTS.

To determine a specific role for the *Pnoc*^{CeA} network in HFD consumption and positive valence, we assessed the impact of activation using optogenetics (Tye and Deisseroth, 2012; Zhang et al., 2007). In separate cohorts of animals, we injected *Pnoc*$^{IRES\text{-}Cre}$ animals with an AAV encoding a Cre-dependent ChR2 and implanted chronic implantable optical fibers over the CeA, vBNST, PBN, and NTS (Sparta et al., 2011; Figures 6B, 6H, 6N, and 6T). *Post hoc* histological verification of these animals revealed a similar pattern of ChR2 expression as we observed with Synaptophysin-mCherry anterograde tracing and accurate fiber placement (Figures 6C, 6I, 6O, 6U, and S5C–S5F).

To measure the impact of *Pnoc*^{CeA} network activation on reward, we assessed performance in two common reward-seeking behaviors. In the real-time place-preference (RTPP)

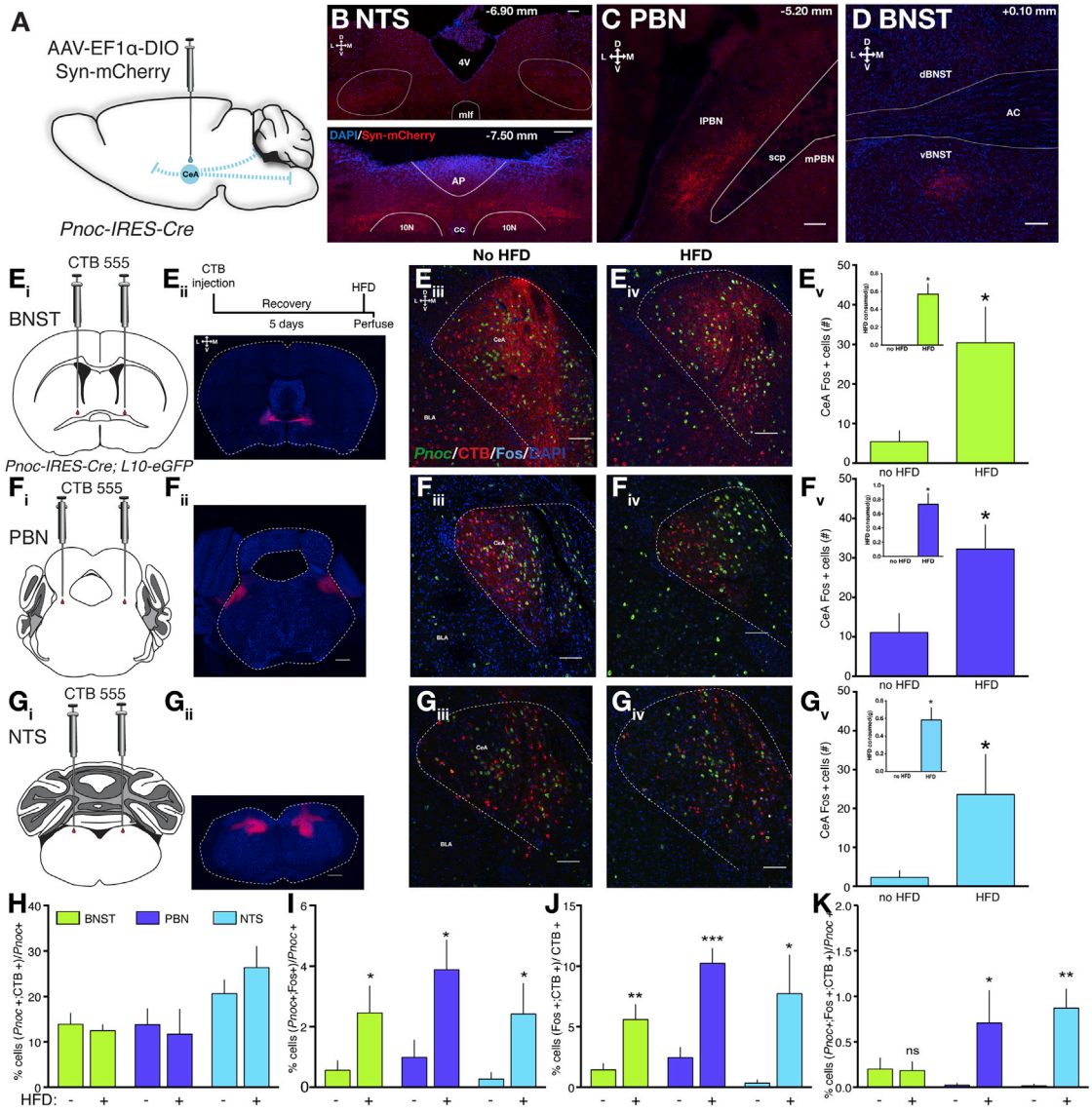

Figure 5. *Pnoc*^{CeA} Neurons Project to the vBNST, PBN, and NTS, and PBN/NTS-Projecting Cells Are Activated following HFD Consumption

(A) Scheme of injection of Cre-dependent Synaptophysin-mCherry anterograde tracer in *Pnoc*$^{IRES\text{-}Cre}$ mice.

(B) Synaptophysin-mCherry immunostaining in anterior and posterior segments of the NTS.

(C) Synaptophysin-mCherry immunostaining in the ventrolateral portion of the PBN.

(D) Synaptophysin-mCherry immunostaining in the ventral BNST.

($E_{i–iv}$) Schematics and example images for CTB injection into the BNST. Top right inset depicts the experimental timeline. (E_v) HFD consumption from BNST-injected animals (inset, p = 0.0006) and overall CeA Fos counts (p = 0.0148).

($F_{i–iv}$) Schematics and example images for CTB injection into the PBN. (F_v) HFD consumption from PBN-injected animals (inset, p = 0.0005) and overall CeA Fos counts (p = 0.0140).

($G_{i–iv}$) Schematics and example images for CTB injection into the NTS. (G_v) HFD consumption from NTS-injected animals (inset, p = 0.0027) and overall CeA Fos counts (p = 0.04404).

(H) Percent of *Pnoc* cells that are colabeled with retrograde CTB.

(I) Percent of *Pnoc* cells colabeled with *Fos* in naive versus HFD-fed animals. p = 0.0393, 0.0152, and 0.0414 for BNST, PBN, and NTS-injected cohort.

(J) Percent of CTB cells colabeled with *Fos* in naive versus HFD-fed animals. p = 0.007, 0.0005, and 0.03 for BNST, PBN, and NTS-injected cohorts.

(K) Percent of *Pnoc* cells colabeled with CTB and Fos. p = 0.4604, 0.0329, and 0.0034 for BNST, PBN, and NTS-injected cohorts, respectively.

For (E_v), (F_v), (G_v), and (H)–(K), data were analyzed using a one-tailed Student's t test between no HFD and HFD conditions within a group of animals with BNST, PBN, or NTS injections where *p < 0.05, **p < 0.01, and ***p < 0.001. For (B)–(D), (E_{iii}), (E_{iv}), (F_{iii}), (F_{iv}), (G_{iii}), and (G_{iv}), scale bars equal 100 μM and 50 μM, respectively. For (E_{ii}), (F_{ii}), and (G_{ii}), scale bars equal 500 μM. Group n's are BNST (HFD: 5; no HFD: 5); PBN (HFD: 4; no HFD: 5); and NTS (HFD: 4; no HFD: 4)

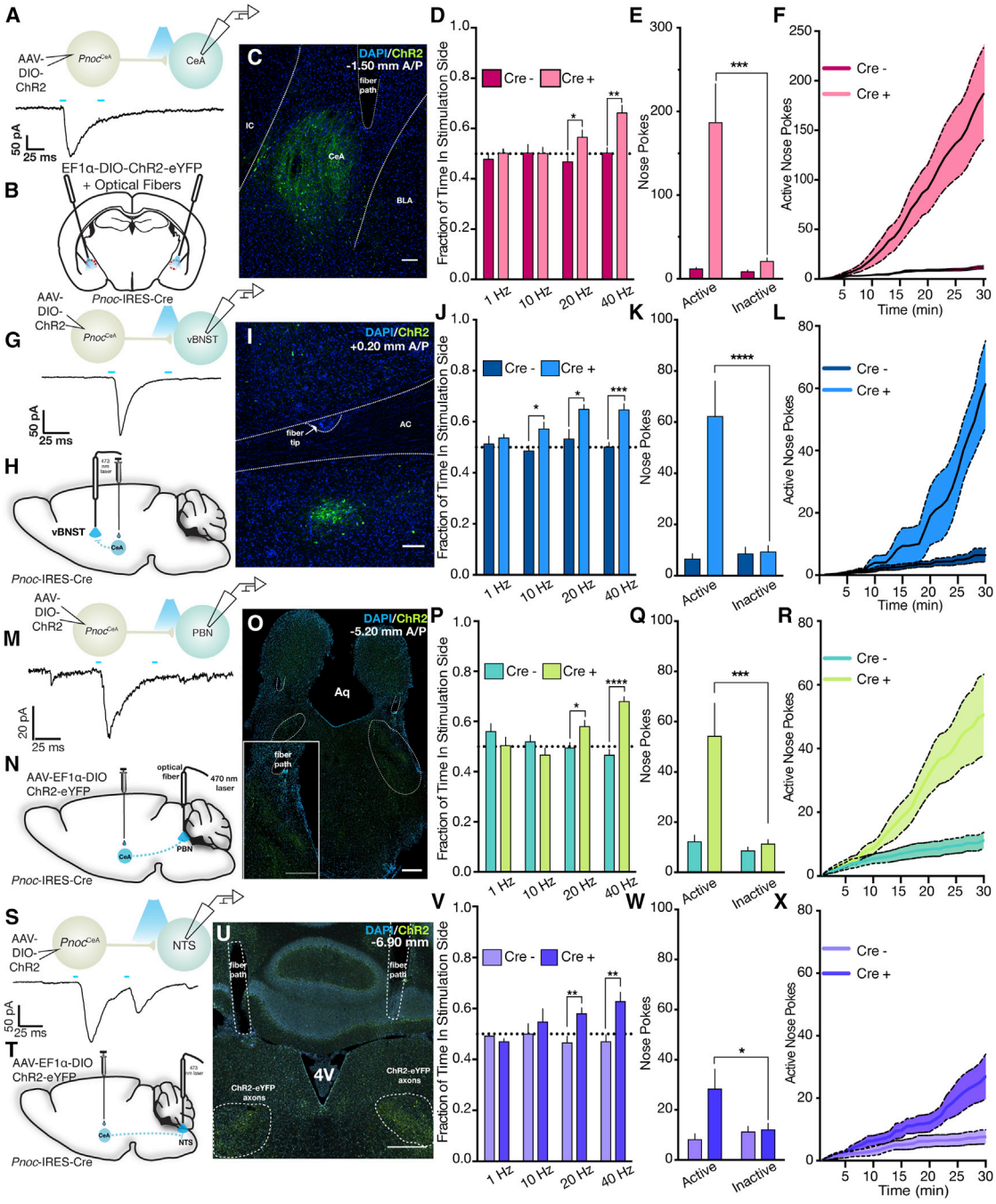

Figure 6. Activation of *Pnoc*^{CeA} Networks Is Reinforcing

(A) Top: schematic of *ex vivo* electrophysiological recordings in the CeA. Bottom: example trace from non-ChR2-expressing cell in the CeA shows a light-evoked (5 ms paired pulse) iPSC.

(B) Schematic showing viral injection and optical fiber placement over the CeA in *Pnoc*$^{IRES\text{-}Cre}$ mice.

(C) Example image showing ChR2-eYFP expression and optical fiber path in the CeA of *Pnoc*$^{IRES\text{-}Cre}$ mice. See Figure S5DDD for complete optical fiber placements.

(D) CeA real-time place-preference behavior over increasing stimulation frequencies (n = 8 Cre− mice and 11 Cre+ mice; unpaired Student's t test; p = 0.3606, 0.9657, 0.037, and 0.0011 at 1, 10, 20, and 40 Hz, respectively).

(E) Total active or inactive port nose pokes during optogenetic self-stimulation sessions at 40 Hz (n = 8 Cre− mice and 11 Cre+ mice; two-way repeated-measures ANOVA with Sidak's multiple comparisons test; group × port interaction; $F_{(1,17)} = 8.035$; p = 0.0114).

(F) Cumulative active port nose pokes across the 40-Hz self-stimulation session (n = 8 Cre− mice and 11 Cre+ mice; two-way repeated-measures ANOVA with Sidak's multiple comparisons test; group × time interaction; $F_{(29,493)} = 9.056$; $p < 0.0001$).

(legend continued on next page)

assay, we found that stimulation of either cell bodies or outputs to vBNST, PBN, or NTS produces a frequency-dependent preference for the stimulation side (Figures 6D, 6J, 6P, and 6V). In the case of cell body, PBN, or NTS stimulation, frequencies of 1 and 10 Hz did not produce a preference, but frequencies of 20 or 40 Hz produced a significant preference for the side paired with optogenetic stimulation. For the vBNST output, we observed a strong preference for high frequencies and a subtle preference for stimulation at 10 Hz, but not 1 Hz (Figure 6J). Similarly, we tested whether mice would nose poke for optogenetic stimulation at either low (10 Hz) or high frequencies (40 Hz). Similar to what we observed with RTPP, we found that mice would nose poke for optogenetic stimulation at 40 Hz (Figures 6E and 6F, 6K and 6L, 6Q and 6R, and 6W and 6X), but not 10 Hz for the vBNST, PBN, and NTS outputs (Figures S5H–S5J). However, we observed that mice would nose poke for stimulation of *Pnoc*^{CeA} cell bodies at 10 Hz (Figure S5G). At 40 Hz, we observed a significant increase in the number of nose pokes for the active laser-paired port relative to the inactive unpaired port in ChR2-expressing animals, but not Cre− controls. Cumulative plots of active port nose pokes revealed a significant increase in the number of active port pokes in the last 10 min of the session for cell body and PBN stimulation and last 5 min for vBNST and NTS stimulation (Figures 6F, 6L, 6R, and 6X). These data clearly demonstrate that frequency-dependent activation of *Pnoc*^{CeA} soma in the CeA or axon terminals in the vBNST, PBN, or NTS is reinforcing and produces reward-like behavior.

To determine the impact of *Pnoc*^{CeA} network activation on feeding and palatable food consumption, we measured feeding behavior in the mouse home cage in combination with *in vivo* optogenetic stimulation. Activation of *Pnoc*^{CeA} cell bodies at 5 Hz had no impact on chow consumption following food deprivation (Figure S5K) or HFD consumption (Figure S5L). Interestingly, activation at 20 Hz decreased chow consumption following food deprivation (Figure S5M). Hand scoring of video recordings revealed that ChR2-expressing animals spent less time interacting with a food pellet (Figures S5N–S5Q), less time chewing on the food pellet (Figures S5R–S5T), and more time engaged in false or fictive feeding behavior (Figures S5U–S5W), where the animals reached their paws toward their mouth as if they were holding food and made chewing-like movements. For the vBNST cohort, using high-frequency stimulation, we found no change in chow consumption following food deprivation (Figure S5X) and a decrease in HFD consumption on the 2nd exposure, but not the 1st exposure (Figures S5Y and S5Z). Likewise, we observed no significant effects on chow consumption following food deprivation with stimulation of either the PBN or NTS pathways (Figures S5AA and S5DD). Surprisingly, we observed no significant effects of either PBN or NTS pathway activation on either the first or second exposure to HFD (Figures S5AA and S5BB and S5DD and S5EE).

It is possible that the lack of effect of optogenetic stimulation on feeding could be driven by increases in anxiety, as previous work has found that activation of hindbrain projections from CeA corticotrophin-releasing factor neurons can drive anxiety

(G) Top: schematic of *ex vivo* electrophysiological recordings in the vBNST. Bottom: example trace from non-ChR2-expressing cell in the vBNST shows a light evoked (5-ms paired pulse) iPSC.
(H) Schematic showing viral injection and optical fiber placement over the vBNST in *Pnoc*$^{IRES-Cre}$ mice.
(I) Example image showing ChR2-eYFP expression and optical fiber path in the vBNST of *Pnoc*$^{IRES-Cre}$ mice. See Figure S5EEE for complete optical fiber placements.
(J) vBNST real-time place-preference behavior over increasing stimulation frequencies (n = 11 Cre− mice and 9 Cre+ mice; unpaired Student's t test; p = 0.5133, 0.0191, 0.0174, and 0.0002 at 1, 10, 20, and 40 Hz, respectively).
(K) Total active or inactive port nose pokes during optogenetic self-stimulation sessions at 40 Hz (n = 11 Cre− mice and 9 Cre+ mice; two-way repeated-measures ANOVA with Sidak's multiple comparisons test; group × port interaction; $F_{(1,18)} = 24.19$; p = 0.0001).
(L) Cumulative active port nose pokes across the 40-Hz self-stimulation session (n = 11 Cre− mice and 9 Cre+ mice; two-way repeated-measures ANOVA with Sidak's multiple comparisons test; group × time interaction; $F_{(29,522)} = 12.10$; p < 0.0001).
(M) Top: schematic of *ex vivo* electrophysiological recordings in the PBN. Bottom: example trace from non-ChR2-expressing cell in the PBN shows a light-evoked (5-ms paired pulse) iPSC.
(N) Schematic showing viral injection and optical fiber placement over the PBN in *Pnoc*$^{IRES-Cre}$ mice.
(O) Example image showing ChR2-eYFP expression and optical fiber path in the PBN of *Pnoc*$^{IRES-Cre}$ mice. See Figure S5FFF for complete optical fiber placements.
(P) PBN real-time place-preference behavior over increasing stimulation frequencies (n = 11 Cre− mice and 12 Cre+ mice; unpaired Student's t test; p = 0.1396, 0.1731, 0.0262, and <0.0001 at 1, 10, 20, and 40 Hz, respectively).
(Q) Total active or inactive port nose pokes during optogenetic self-stimulation sessions at 40 Hz (n = 11 Cre− mice and 12 Cre+ mice; two-way repeated-measures ANOVA with Sidak's multiple comparisons test; group × port interaction; $F_{(1,21)} = 7.849$; p = 0.0107).
(R) Cumulative active port nose pokes across the 40-Hz self-stimulation session (n = 11 Cre− mice and 12 Cre+ mice; two-way repeated-measures ANOVA with Sidak's multiple comparisons test; group × time interaction; $F_{(29,609)} = 8.066$; p < 0.0001).
(S) Top: schematic of *ex vivo* electrophysiological recordings in the NTS. Bottom: example trace from non-ChR2-expressing cell in the NTS shows a light evoked (5-ms paired pulse) iPSC.
(T) Schematic showing viral injection and optical fiber placement over the NTS in *Pnoc*$^{IRES-Cre}$ mice.
(U) Example image showing ChR2-eYFP expression and optical fiber path in the NTS of *Pnoc*$^{IRES-Cre}$ mice. See Figure S5GGG for complete optical fiber placements.
(V) NTS real-time place-preference behavior over increasing stimulation frequencies (n = 9 Cre− mice and 12 Cre+ mice; unpaired Student's t test; p = 0.2327, 0.5079, 0.0044, and 0.0043 at 1, 10, 20, and 40 Hz, respectively).
(W) Total active or inactive port nose pokes during optogenetic self-stimulation sessions at 40 Hz (n = 9 Cre− mice and 12 Cre+ mice; two-way repeated-measures ANOVA with Sidak's multiple comparisons test; group × port interaction; $F_{(1,19)} = 6.327$; p = 0.0211).
(X) Cumulative active port nose pokes across the 40-Hz self-stimulation session (n = 9 Cre− mice and 12 Cre+ mice; two-way repeated-measures ANOVA with Sidak's multiple comparisons test; group × time interaction; $F_{(29,551)} = 8.066$; p < 0.0001).

and aversion (McCall et al., 2015). To address this, we assessed the contribution of *Pnoc*^{CeA} neuron networks to anxiety. Similar to our chemogenetic hM4D findings, optogenetic activation of neither *Pnoc*^{CeA} cell bodies nor their projections to the vBNST, PBN, or NTS were sufficient to produce anxiety-like phenotypes as revealed by the open field assay (Figures S5FF and S5GG, S5MM and S5NN, S5TT and S5UU, and S5AAA and S5BBB), elevated plus maze (Figures S5HH–S5JJ, S5OO–S5QQ, S5VV–S5XX, and S5CCC–S5EEE), or novelty-induced suppression of feeding (Figures S5KK and S5LL, S5RR and S5SS, S5YY and S5ZZ, and S5FFF and S5GG) assays. In the open field assay, we observed no differences in center time across all of the groups (Figures S5GG, S5MM, S5TT, and S5AAA). Interestingly, we observed reductions in the distance traveled of an open field during the third epoch of blue light stimulation with cell body or PBN activation (Figures S5FF and S5TT), but not vBNST or NTS activation (Figures S5MM and S5AA). In the elevated plus maze, we observed no significant differences in the distance traveled, open arm time, or the probability of an open arm entry across all cohorts (Figures S5HH–S5JJ, S5OO–S5QQ, S5VV–S5XX, and S5CCC–S5EEE). In the novelty-induced suppression of feeding assay, we observed no significant differences in the latency to feed or home cage consumption of fruit loops (Figures S5KK and S5LL, S5RR and S5SS, S5YY and S5ZZ, and S5FFF and S5GGG). These data are consistent with a lack of anxiogenesis produced by optogenetic stimulation of the *Pnoc*^{CeA} neural networks.

DISCUSSION

In this study, we used a newly created Prepronociceptin-Cre mouse line combined with multiple genetic, electrophysiological, and behavioral approaches to identify new CeA circuits necessary for regulation of hedonic feeding, but not homeostatic feeding or anxiety. The CeA has been intensely investigated, mainly for its role in aversive behaviors. Consistent with our findings, emerging studies have demonstrated that CeA can also play a role in driving reward-related behaviors. However, this is the first study to ascribe specific hedonic feeding actions to a subpopulation of CeA neurons. We provide the first demonstration that genetic manipulation of a population of CeA neurons can mitigate diet-induced obesity. Furthermore, our identification of *Pnoc*^{CeA} provides novel insight into the pathology of binge eating of calorically dense, palatable food.

Our functional studies using viral-mediated ablation of *Pnoc*^{CeA} cells reveal a highly specific role for *Pnoc*^{CeA} cells in cumulative palatable HFD consumption over the course of 5 intermittent access sessions or 3 days of continuous HFD access as well as in a chronic model of HFD consumption. Additionally, our caspase ablation experiments revealed that ablation of *Pnoc*^{CeA} neurons reduced changes in physiology that accompany short-term-HFD-exposure-related increases in bodyweight, body fat mass, respiratory exchange, and core body temperature. For food consumption, the effect of CeA lesions on food intake and bodyweight have been very mixed (Rollins and King, 2000), with some experiments showing hyperphagia and obesity. Our experiments strengthen the proposed role of CeA cellular networks in *promoting* food intake in general and palatable food specifically. Ablation of *Pnoc*^{CeA} cells also reduced 24-h, 2-bottle choice preference for saccharin, but not sucrose. Intriguingly, we found that aversion to high concentrations of quinine was enhanced. These data also exclude a general role for *Pnoc* neurons in salience detection, as we would have observed a reduced aversion to quinine. We speculate that *Pnoc* neurons are activated during consumption of aversive foods (as we observed in our optical tagging data) in order to balance avoidance and approach. Collectively, these results suggest that *Pnoc*^{CeA} neurons are a cellular node that promotes consumption of palatable foods and the development of high-fat-diet-induced obesity. Although our Fos and electrophysiological data show that acute palatable food exposure activates *Pnoc*^{CeA} cells, future studies are necessary to understand how long-term exposure and the development of obesity alters neuronal activity of these cells and plasticity in the *Pnoc*^{CeA} connectivity to other brain regions.

Similar to our caspase experiments, we observed that chemogenetic inhibition reduced home cage HFD consumption without producing anxiety-like behavior. Notably, we only observed this effect on the animal's first exposure to the HFD or when combined with a stressor like a change of the home cage bedding. In agreement with these observations and the effect of *Pnoc*^{CeA} cell ablation on HFD consumption, we observed that chemogenetic inhibition of *Pnoc*^{CeA} cells reduced fruit loop consumption in the novelty-induced suppression of feeding assay. Similarly to solid food intake, we examined whether acute inhibition of *Pnoc*^{CeA} neurons impacts aversive or palatable liquid tastant intake. We did not observe any significant change in fluid intake in general or aversive or palatable tastant intake specifically. For palatable tastants, there was no difference in the effect of inhibition under conditions of novelty or familiarity. We speculate that there are potentially a few factors in play here. One is that ablation and chemogenetic inhibition experiments produce behavioral effects at different timescales. Two is that an enhancement in quinine aversion or reductions in palatable tastant intake might have been technically limited by the amount of intake in these acute assays, where the overall intake is much lower than in a 24-h assay, creating a floor effect. Furthermore, if *Pnoc*^{CeA} neurons are encoding valence information about the tastant, it is possible that shorter exposures like 1 h do not allow for the encoding of tastant valence to manifest themselves behaviorally in this case. Although we cannot rule out additional circuit level compensatory effects that might accompany ablation versus chemogenetic inhibition, together, these data argue for an important role for *Pnoc*^{CeA} cells in promoting palatable food intake.

One possibility is that initial exposure to palatable foods, stressors, and a recent exposure to a novel arena all require increased motivation from animals to produce feeding. This model is supported by recent work from the Palmiter group suggesting that the initial exposure to HFD engages PBN CGRP neuron activation (Campos et al., 2018). Optogenetic stimulation of the CeA or injection of μ-opioid receptor agonists into the CeA in rats was shown to increase incentive salience for and shape operant responding for sucrose rewards (Mahler and Berridge, 2009; Robinson et al., 2014). *Pnoc*^{CeA} cells may be a neuronal subset of the CeA that functions to narrow incentive motivation

or assign positive valence to palatable foods. Finally, it is possible that, if *Pnoc*^{CeA} cells encode information regarding the valence of a stimulus, then a transient inhibition by CNO may not allow for differential encoding of tastant preference to manifest behaviorally.

Whereas ablation and chemogenetic inhibition of *Pnoc*^{CeA} neurons reduced palatable food consumption, optogenetic activation of either *Pnoc* cell bodies or outputs to the vBNST, PBN, or NTS pathway had minimal effects on home cage feeding of either chow or HFD. However, optogenetic stimulation of *Pnoc*^{CeA} neurons and outputs to the vBNST, PBN, and NTS pathways revealed high-frequency-dependent reward-like behavior using the real-time place preference and operant optogenetic self-stimulation assays. We hypothesize that there may be separable encoding of the rewarding, reinforcing, and consummatory aspects of palatable food to the vBNST, PBN, and NTS or other brain regions.

Calca (CGRP) neurons in the lateral portion of the parabrachial nucleus (*Calca*^{PBN}) are known to be anorexigenic, so we were surprised that optogenetic activation of an inhibitory pathway to the PBN did not increase food intake. Carter et al. (2013) noted that inhibition of *Calca*^{PBN} neurons only increased food intake when animals normally did not eat, for example, following the injection of anorexigenic agents. Similarly, Campos et al. (2016) showed that long-term inactivation with tetanus toxin did not affect long-term chow intake or bodyweight but that inactivation of *Calca*^{PBN} cells produced a 3-fold increase in palatable liquid diet consumption. Another possibility is that *Pnoc*^{CeA} cells make functional synapses with non-CGRP cells in the PBN. Overall, future studies using single-cell gene expression in combination with *ex vivo* slice electrophysiology will be necessary to determine the identity of postsynaptic vBNST, PBN, and NTS cells.

Pnoc^{CeA} cells only minimally overlap with PKCδ (*Prkcd*), *Crh*, *Nts*, *Calcr*, *Tac2*, and *Htr2a* neurons and have modest overlap with SST neurons. Both PKCδ and SST neurons form an antagonistic local network for coordinating learned fear responses (Haubensak et al., 2010; Li et al., 2013). In the latter case, optogenetic activation of *Sst*^{CeA} neurons at high frequencies promotes freezing behavior in response to a conditioned stimulus paired with a foot shock in naive mice, and optogenetic inhibition blocked the acquisition of cue-fear learning 24 h after learning. Our data clearly demonstrate that chemogenetic inhibition of *Pnoc*^{CeA} cells in several anxiety assays revealed a general increase in locomotory behavior and that optogenetic activation of *Pnoc*^{CeA} neurons and outputs showed a subtle decrease in distance traveled in the open field. Combined with recent data showing a role for the CeA in locomotory pursuit of prey (Han et al., 2017), this suggests that the CeA may have a broader, underappreciated role in the control of locomotory behavior. Han et al. also observed that chemogenetic activation or inhibition of vesicular GABA transporter (vGAT)-expressing cells in the CeA had no effect on feeding but that optogenetic activation of vGAT cells induced mastication of non-food objects and that optogenetic activation of CeA ChR2 axons in the reticular formation of the brain stem could induce fictive feeding, even in the absence of prey animals or available food. Recently, Douglass et al. (2017) found that *Htr2a*-expressing CeA cells are activated during food intake and that optogenetic and chemogenetic activation of *Htr2a* neurons promotes ongoing food intake through a reinforcing positive valence signal. We observed only minimal overlap of *Pnoc* and *Htr2a* in the CeA and, overall, observed a very low abundance of *Htr2a* mRNA in the CeA, but our data and others are consistent with the encoding of positive valence in multiple CeA subtypes (Kim et al., 2017). Opposite of our prediction, optogenetic activation at frequencies of *Pnoc* neurons that were rewarding depressed feeding while also producing non-specific fictive feeding. This is consistent with a recent study using hM3D DREADD activation of the CeM in rats (Zséli et al., 2018). Our data are more consistent with the role of reward in producing satiation or that subsets of *Pnoc* cells may contribute to promoting appetitive behavior and satiation possibly through distinct local and output networks. Lastly, we advise caution in interpreting sufficiency (not necessity) of the contribution of specific neural circuits to feeding when their optogenetic activation produces motor patterns of eating across a broad consummatory spectrum (Burnett et al., 2016; Navarro et al., 2016).

STAR★METHODS

Detailed methods are provided in the online version of this paper and include the following:

- KEY RESOURCES TABLE
- CONTACT FOR REAGENT AND RESOURCE SHARING
- EXPERIMENTAL MODEL AND SUBJECT DETAILS
  - Animals
  - Development of Pnoc-IRES-Cre mouse strain
- METHOD DETAILS
  - Tissue processing
  - Immunohistochemistry and dual fluorescence *in situ* hybridization
  - Virus Injections and Survival Surgery
  - iDISCO+ protocol
  - Feeding and Calorimetric Measurements
  - *In vivo* electrophysiology and optical tagging of Pnoc^{CeA} neurons
  - Slice Electrophysiology
  - Chemogenetic and Optogenetic Behaviors
- QUANTIFICATION AND STATISTICAL ANALYSIS

SUPPLEMENTAL INFORMATION

Supplemental Information can be found online at https://doi.org/10.1016/j.neuron.2019.03.037.

ACKNOWLEDGMENTS

J.A.H. was funded by T32-MH076694 and DK115902. C.M.M. was funded by F31 AA023440 from the National Institute on Alcohol Abuse and Alcoholism. T.L.K. was funded by P60 AA011605, R01 AA019454, U01 AA020911, and U01 MH105892. M.R.B. was funded by DA034929 and MH112355. Calorimetry experiments were performed in the UNC Animal Metabolism Phenotyping Core funded by DK056350. We would also like to acknowledge assistance from Kunjie Hua. C.M.B. acknowledges funding from the Swedish Research Council (VR Dnr: 538-2013-8864). The UNC Microscopy Services Laboratory, Department of Pathology and Laboratory Medicine, is supported in part by P30 CA016086 Cancer Center Core Support Grant to the UNC Lineberger

Comprehensive Cancer Center. Research reported in this publication was supported in part by the North Carolina Biotechnology Center Institutional Support Grant 2016-IDG-1016.

AUTHOR CONTRIBUTIONS

J.A.H. and T.L.K. designed the experiments with consultation from A.H., L.R.H., C.M.B., and M.P.S. J.A.H., L.R.H., C.M.M., D.P., M.K., J.F.D., J.J., A.S., J.A.S., K.M.B., O.J.H., S.N., A.E., C.M.S., and G.T. performed experiments. J.A.H., L.R.H., and T.L.K. analyzed all data and wrote the manuscript. Z.M., M.R.B., T.C.J., and G.D.S. contributed reagents for the paper.

DECLARATION OF INTERESTS

The authors declare no competing interests.

Received: January 27, 2017
Revised: September 27, 2018
Accepted: March 27, 2019
Published: April 24, 2019; corrected online: May 4, 2019

REFERENCES

Amano, T., Amir, A., Goswami, S., and Paré, D. (2012). Morphology, PKCδ expression, and synaptic responsiveness of different types of rat central lateral amygdala neurons. J. Neurophysiol. *108*, 3196–3205.

Armbruster, B.N., Li, X., Pausch, M.H., Herlitze, S., and Roth, B.L. (2007). Evolving the lock to fit the key to create a family of G protein-coupled receptors potently activated by an inert ligand. Proc. Natl. Acad. Sci. USA *104*, 5163–5168.

Berthoud, H.R., Lenard, N.R., and Shin, A.C. (2011). Food reward, hyperphagia, and obesity. Am. J. Physiol. Regul. Integr. Comp. Physiol. *300*, R1266–R1277.

Burnett, C.J., Li, C., Webber, E., Tsaousidou, E., Xue, S.Y., Brüning, J.C., and Krashes, M.J. (2016). Hunger-driven motivational state competition. Neuron *92*, 187–201.

Cai, H., Haubensak, W., Anthony, T.E., and Anderson, D.J. (2014). Central amygdala PKC-δ(+) neurons mediate the influence of multiple anorexigenic signals. Nat. Neurosci. *17*, 1240–1248.

Campos, C.A., Bowen, A.J., Schwartz, M.W., and Palmiter, R.D. (2016). Parabrachial CGRP neurons control meal termination. Cell Metab. *23*, 811–820.

Campos, C.A., Bowen, A.J., Roman, C.W., and Palmiter, R.D. (2018). Encoding of danger by parabrachial CGRP neurons. Nature *555*, 617–622.

Carter, M.E., Soden, M.E., Zweifel, L.S., and Palmiter, R.D. (2013). Genetic identification of a neural circuit that suppresses appetite. Nature *503*, 111–114.

Carter, M.E., Han, S., and Palmiter, R.D. (2015). Parabrachial calcitonin gene-related peptide neurons mediate conditioned taste aversion. J. Neurosci. *35*, 4582–4586.

Chieng, B.C.H., Christie, M.J., and Osborne, P.B. (2006). Characterization of neurons in the rat central nucleus of the amygdala: cellular physiology, morphology, and opioid sensitivity. J. Comp. Neurol. *497*, 910–927.

Ciccocioppo, R., Fedeli, A., Economidou, D., Policani, F., Weiss, F., and Massi, M. (2003). The bed nucleus is a neuroanatomical substrate for the anorectic effect of corticotropin-releasing factor and for its reversal by nociceptin/orphanin FQ. J. Neurosci. *23*, 9445–9451.

D'Agostino, G., Lyons, D.J., Cristiano, C., Burke, L.K., Madara, J.C., Campbell, J.N., Garcia, A.P., Land, B.B., Lowell, B.B., Dileone, R.J., and Heisler, L.K. (2016). Appetite controlled by a cholecystokinin nucleus of the solitary tract to hypothalamus neurocircuit. eLife *5*, e12225.

Douglass, A.M., Kucukdereli, H., Ponserre, M., Markovic, M., Gründemann, J., Strobel, C., Alcala Morales, P.L., Conzelmann, K.-K., Lüthi, A., and Klein, R. (2017). Central amygdala circuits modulate food consumption through a positive-valence mechanism. Nat. Neurosci. *20*, 1384–1394.

Fadok, J.P., Markovic, M., Tovote, P., and Lüthi, A. (2018). New perspectives on central amygdala function. Curr. Opin. Neurobiol. *49*, 141–147.

Gilpin, N.W., Herman, M.A., and Roberto, M. (2015). The central amygdala as an integrative hub for anxiety and alcohol use disorders. Biol. Psychiatry *77*, 859–869.

Gray, T.S., and Magnuson, D.J. (1987). Neuropeptide neuronal efferents from the bed nucleus of the stria terminalis and central amygdaloid nucleus to the dorsal vagal complex in the rat. J. Comp. Neurol. *262*, 365–374.

Han, W., Tellez, L.A., Rangel, M.J., Jr., Motta, S.C., Zhang, X., Perez, I.O., Canteras, N.S., Shammah-Lagnado, S.J., van den Pol, A.N., and de Araujo, I.E. (2017). Integrated control of predatory hunting by the central nucleus of the amygdala. Cell *168*, 311–324.e18.

Hardaway, J.A., Crowley, N.A., Bulik, C.M., and Kash, T.L. (2015). Integrated circuits and molecular components for stress and feeding: implications for eating disorders. Genes Brain Behav. *14*, 85–97.

Hardaway, J.A., Jensen, J., Kim, M., Mazzone, C.M., Sugam, J.A., Diberto, J.F., Lowery-Gionta, E.G., Hwa, L.S., Pleil, K.E., Bulik, C.M., and Kash, T.L. (2016). Nociceptin receptor antagonist SB 612111 decreases high fat diet binge eating. Behav. Brain Res. *307*, 25–34.

Hariri, N., and Thibault, L. (2010). High-fat diet-induced obesity in animal models. Nutr. Res. Rev. *23*, 270–299.

Haubensak, W., Kunwar, P.S., Cai, H., Ciocchi, S., Wall, N.R., Ponnusamy, R., Biag, J., Dong, H.-W., Deisseroth, K., Callaway, E.M., et al. (2010). Genetic dissection of an amygdala microcircuit that gates conditioned fear. Nature *468*, 270–276.

Ikeda, K., Watanabe, M., Ichikawa, T., Kobayashi, T., Yano, R., and Kumanishi, T. (1998). Distribution of prepro-nociceptin/orphanin FQ mRNA and its receptor mRNA in developing and adult mouse central nervous systems. J. Comp. Neurol. *399*, 139–151.

Jais, A., Solas, M., Backes, H., Chaurasia, B., Kleinridders, A., Theurich, S., Mauer, J., Steculorum, S.M., Hampel, B., Goldau, J., et al. (2016). Myeloid-cell-derived VEGF maintains brain glucose uptake and limits cognitive impairment in obesity. Cell *165*, 882–895.

Kim, J., Zhang, X., Muralidhar, S., LeBlanc, S.A., and Tonegawa, S. (2017). Basolateral to central amygdala neural circuits for appetitive behaviors. Neuron *93*, 1464–1479.e5.

Kovacs, K.M., Szakall, I., O'Brien, D., Wang, R., Vinod, K.Y., Saito, M., Simonin, F., Kieffer, B.L., and Vadasz, C. (2005). Decreased oral self-administration of alcohol in kappa-opioid receptor knock-out mice. Alcohol. Clin. Exp. Res. *29*, 730–738.

Krashes, M.J., Koda, S., Ye, C., Rogan, S.C., Adams, A.C., Cusher, D.S., Maratos-Flier, E., Roth, B.L., and Lowell, B.B. (2011). Rapid, reversible activation of AgRP neurons drives feeding behavior in mice. J. Clin. Invest. *121*, 1424–1428.

Li, H., Penzo, M.A., Taniguchi, H., Kopec, C.D., Huang, Z.J., and Li, B. (2013). Experience-dependent modification of a central amygdala fear circuit. Nat. Neurosci. *16*, 332–339.

Mahler, S.V., and Berridge, K.C. (2009). Which cue to "want?" Central amygdala opioid activation enhances and focuses incentive salience on a prepotent reward cue. J. Neurosci. *29*, 6500–6513.

McCall, J.G., Al-Hasani, R., Siuda, E.R., Hong, D.Y., Norris, A.J., Ford, C.P., and Bruchas, M.R. (2015). CRH engagement of the locus coeruleus noradrenergic system mediates stress-induced anxiety. Neuron *87*, 605–620.

Moga, M.M., and Gray, T.S. (1985). Evidence for corticotropin-releasing factor, neurotensin, and somatostatin in the neural pathway from the central nucleus of the amygdala to the parabrachial nucleus. J. Comp. Neurol. *241*, 275–284.

Navarro, M., Olney, J.J., Burnham, N.W., Mazzone, C.M., Lowery-Gionta, E.G., Pleil, K.E., Kash, T.L., and Thiele, T.E. (2016). Lateral hypothalamus GABAergic neurons modulate consummatory behaviors regardless of the caloric content or biological relevance of the consumed stimuli. Neuropsychopharmacology *41*, 1505–1512.

Neal, C.R., Jr., Mansour, A., Reinscheid, R., Nothacker, H.P., Civelli, O., and Watson, S.J., Jr. (1999). Localization of orphanin FQ (nociceptin) peptide

and messenger RNA in the central nervous system of the rat. J. Comp. Neurol. *406*, 503–547.

O'Doherty, J.P., Deichmann, R., Critchley, H.D., and Dolan, R.J. (2002). Neural responses during anticipation of a primary taste reward. Neuron *33*, 815–826.

Opland, D., Sutton, A., Woodworth, H., Brown, J., Bugescu, R., Garcia, A., Christensen, L., Rhodes, C., Myers, M., Jr., and Leinninger, G. (2013). Loss of neurotensin receptor-1 disrupts the control of the mesolimbic dopamine system by leptin and promotes hedonic feeding and obesity. Mol. Metab. *2*, 423–434.

Park, T.H., and Carr, K.D. (1998). Neuroanatomical patterns of fos-like immunoreactivity induced by a palatable meal and meal-paired environment in saline- and naltrexone-treated rats. Brain Res. *805*, 169–180.

Pomonis, J.D., Billington, C.J., and Levine, A.S. (1996). Orphanin FQ, agonist of orphan opioid receptor ORL1, stimulates feeding in rats. Neuroreport *8*, 369–371.

Renier, N., Wu, Z., Simon, D.J., Yang, J., Ariel, P., and Tessier-Lavigne, M. (2014). iDISCO: a simple, rapid method to immunolabel large tissue samples for volume imaging. Cell *159*, 896–910.

Renier, N., Adams, E.L., Kirst, C., Wu, Z., Azevedo, R., Kohl, J., Autry, A.E., Kadiri, L., Umadevi Venkataraju, K., Zhou, Y., et al. (2016). Mapping of brain activity by automated volume analysis of immediate early genes. Cell *165*, 1789–1802.

Robinson, M.J.F., Warlow, S.M., and Berridge, K.C. (2014). Optogenetic excitation of central amygdala amplifies and narrows incentive motivation to pursue one reward above another. J. Neurosci. *34*, 16567–16580.

Rollins, B.L., and King, B.M. (2000). Amygdala-lesion obesity: what is the role of the various amygdaloid nuclei? Am. J. Physiol. Regul. Integr. Comp. Physiol. *279*, R1348–R1356.

Roman, C.W., Derkach, V.A., and Palmiter, R.D. (2016). Genetically and functionally defined NTS to PBN brain circuits mediating anorexia. Nat. Commun. *7*, 11905.

Small, D.M. (2012). Flavor is in the brain. Physiol. Behav. *107*, 540–552.

Small, D.M., Veldhuizen, M.G., Felsted, J., Mak, Y.E., and McGlone, F. (2008). Separable substrates for anticipatory and consummatory food chemosensation. Neuron *57*, 786–797.

Sparta, D.R., Stamatakis, A.M., Phillips, J.L., Hovelsø, N., van Zessen, R., and Stuber, G.D. (2011). Construction of implantable optical fibers for long-term optogenetic manipulation of neural circuits. Nat. Protoc. *7*, 12–23.

Statnick, M.A., Chen, Y., Ansonoff, M., Witkin, J.M., Rorick-Kehn, L., Suter, T.M., Song, M., Hu, C., Lafuente, C., Jiménez, A., et al. (2016). A novel nociceptin receptor antagonist LY2940094 inhibits excessive feeding behavior in rodents: a possible mechanism for the treatment of binge eating disorder. J. Pharmacol. Exp. Ther. *356*, 493–502.

Tye, K.M., and Deisseroth, K. (2012). Optogenetic investigation of neural circuits underlying brain disease in animal models. Nat. Rev. Neurosci. *13*, 251–266.

Valdivia, S., Patrone, A., Reynaldo, M., and Perello, M. (2014). Acute high fat diet consumption activates the mesolimbic circuit and requires orexin signaling in a mouse model. PLoS ONE *9*, e87478.

Wu, Q., Lemus, M.B., Stark, R., Bayliss, J.A., Reichenbach, A., Lockie, S.H., and Andrews, Z.B. (2014). The temporal pattern of cfos activation in hypothalamic, cortical, and brainstem nuclei in response to fasting and refeeding in male mice. Endocrinology *155*, 840–853.

Yang, C.F., Chiang, M.C., Gray, D.C., Prabhakaran, M., Alvarado, M., Juntti, S.A., Unger, E.K., Wells, J.A., and Shah, N.M. (2013). Sexually dimorphic neurons in the ventromedial hypothalamus govern mating in both sexes and aggression in males. Cell *153*, 896–909.

Zhang, F., Aravanis, A.M., Adamantidis, A., de Lecea, L., and Deisseroth, K. (2007). Circuit-breakers: optical technologies for probing neural signals and systems. Nat. Rev. Neurosci. *8*, 577–581.

Zséli, G., Vida, B., Szilvásy-Szabó, A., Tóth, M., Lechan, R.M., and Fekete, C. (2018). Neuronal connections of the central amygdalar nucleus with refeeding-activated brain areas in rats. Brain Struct. Funct. *223*, 391–414.

STAR★METHODS

KEY RESOURCES TABLE

REAGENT or RESOURCE	SOURCE	IDENTIFIER
Antibodies		
Rabbit anti *c-fos* (1:3,000)	Santa Cruz Biotechnology	sc-52
Mouse anti-PKC-δ (1:500)	BD Biosciences	610398
Rabbit Somatostatin-14 (1:2,000)	Peninsula Laboratories	T-4103
Mouse anti-TH (1:1,000)	Immunostar	22941
Goat anti CGRP (1:500)	Abcam	ab36001
Rabbit anti-RFP	Rockland Immunochemicals	600-401-379
Bacterial and Virus Strains		
AAV8-hSyn-DIO-hM4d-mCherry	(Krashes et al., 2011)	UNC Vector Core AV4908B/Addgene 44362
AAV8-hSyn-DIO-mCherry	(Krashes et al., 2011)	UNC Vector Core 4981CD
AAV5-EF1a-DIO-ChR2-eYFP	Deisseroth Lab	UNC Vector Core
AAV5-EF1a-DIO-taCasp3-tevP	(Yang et al., 2013)	UNC Vector Core
AAV8.2-EF1a-DIO-Synaptophysin-mCherry	(Opland et al., 2013)	MIT Vector Core
Chemicals, Peptides, and Recombinant Proteins		
Cholera Toxin Subunit B 555	Thermofisher Scientific	C34776
CNO	Gift from Bryan Roth and Hello Bio	HB6149
Critical Commercial Assays		
Tyramide Signal Amplification Kit	Perkin Elmer	NEL701001KT
viewRNA Probes	Affymetrix (now Thermofisher)	NA
Mm-Pnoc	Affymetrix (now Thermofisher)	VB1-3030997-VT
Cre	Affymetrix (now Thermofisher)	VF1-13057
RNAscope Probes	Advanced Cell Diagnostics	NA
Mm-*Pnoc*	Advanced Cell Diagnostics	437881
Mm-*Crh*	Advanced Cell Diagnostics	316091-C2
Mm-*Nts*	Advanced Cell Diagnostics	420441-C2
Mm-*Tac2*	Advanced Cell Diagnostics	446391-C2
Mm-*Calcr*	Advanced Cell Diagnostics	452281-C2
Mm-*Htr2a*	Advanced Cell Diagnostics	401291-C2
Mm-*Prkcd*	Advanced Cell Diagnostics	441791-C2
Mm-*Sst*	Advanced Cell Diagnostics	404631-C2
Experimental Models: Organisms/Strains		
Pnoc-IRES-Cre	This paper	N/A
C57BL6/J	The Jackson Laboratory	Stock #000664
B6.Cg-*Gt(ROSA)26Sor*$^{tm9(CAG\text{-}tdTomato)Hze}$/J	The Jackson Laboratory	Stock #007909
B6.Gt(ROSA)26Sor$^{tm1(CAG\text{-}EGFP/Rpl10)Dolsn}$	Kind gift from Brad Lowell	MGI: 5559562
Software and Algorithms		
Zen Blue Advanced Processing Module	Zeiss	https://www.zeiss.com/microscopy/us/products/microscope-software/zen/image-analysis.html
pClamp/Clampfit 10.7	Molecular Devices	http://mdc.custhelp.com/app/answers/detail/a_id/18779/~/axon™pclamp™-10-electrophysiology-data-acquisition-%26-analysis-software-download
Image processing, cell counter module	ImageJ/Fiji	https://fiji.sc/
Prism 6.0h	Graphpad	https://www.graphpad.com/

(*Continued on next page*)

Continued

REAGENT or RESOURCE	SOURCE	IDENTIFIER
Imaris	Bitplane	https://www.bitplane.com/imaris
Clearmap	(Renier et al., 2016)	https://github.com/ChristophKirst/ClearMap
Omniplex Neural Data Acquisition System/Offline Sorter	Plexon	https://plexon.com/products/omniplex-d-neural-data-acquisition-system-1/

CONTACT FOR REAGENT AND RESOURCE SHARING

Additional information and requests for resources or reagents used in this paper should be directed and will be fulfilled by the Lead Contact, Thomas L. Kash (thomas_kash@med.unc.edu).

EXPERIMENTAL MODEL AND SUBJECT DETAILS

Animals

Adult male C57BL/6J and *Pnoc*$^{IRES\text{-}Cre}$ mice (age 8-24 weeks) were group housed in ventilated cages (Tecniplast) in a colony room on a standard 12:12 h light-dark cycle (lights on at 7 AM) until time of experiments. For long term assessment of *Pnoc*^{CeA} effects on diet-induced obesity, the mice were older at the time of sacrifice. For chemogenetic and optogenetic experiments, we used Cre- cage and littermate controls. Unless otherwise noted animals had *ad libitum* access to food and water. For measurements of food intake, calorimetric assessments, and other behavioral measurements male mice were singly housed. Mice were acclimated to single housing at least a week prior to any measurements or experiments. Food hoppers were fitted with a custom made trapezoidal plexiglas divider to provide access to multiple types of food at once. All procedures were approved by the Institutional Animal Care and Use Committee of the University of North Carolina at Chapel Hill and performed in accordance with the National Institute of Health's guide for the care and use of laboratory animals.

Development of Pnoc-IRES-Cre mouse strain

129 BAC genomic clones containing the *Pnoc* genes was used to target a cassette containing the Cre recombinase gene preceded by an internal ribosomal entry sequence (IRES-Cre) just downstream of the *Pnoc* stop codon, respectively so that Cre recombinase expression was driven by the endogenous *Pnoc* genes. The *Pnoc*-IRES-Cre targeting constructs were electroporated into W4 ES cells, and screened using an FRT-flanked neo-cassette. Targeted clones were injected into blastocysts. Chimeras were obtained and bred for germline transmission of the *Pnoc*-IRES-Cre allele. Following germline transmission, *Pnoc*-IRES-cre mice were crossed to Rosa-FLPR mice to remove the neo cassette at the 3′end of the IRES-cre sequence.

METHOD DETAILS

Tissue processing

Unless otherwise stated, animals were transcardially perfused with 0.01 M phosphate-buffered saline (PBS) and then 50 mL 4% paraformaldehyde (PFA). Brains were dissected and post-fixed in 4% PFA overnight and then transferred to 30% w/v sucrose solution for cryoprotection. Brains were sectioned at 40 μM on a cryostat and stored in a 50/50 PBS/glycerol solution at −20. Brain sections were used for downstream applications like immunohistochemistry and tracing. For behavioral cohorts, the presence of fluorescent transgenes and optical fiber placements was confirmed before ultimate inclusion in the presented datasets.

Immunohistochemistry and dual fluorescence *in situ* hybridization

Quantification of Prepronociceptin and PKCδ/Somatostatin Coexpression

Male *Pnoc*$^{IRES\text{-}Cre}$; Ai9 (TdTomato) mice were perfused and cryosectioned using standard protocols. Sections from the entire anterior-posterior range of the CeA were stained using an antibody specific to PKC-δ (BD Biosciences – 610398, 1: 500) or Somatostatin (Peninsula Laboratories – T-4103, 1: 2,000) (Figure S2). Briefly, sections were washed, permeabilized in 0.5% Triton X-100/PBS for 30 min, washed, and blocked in 10% NDS/1% bovine serum albumin (BSA)(w/v)/0.1% Triton X-100/PBS for 1 hour. Primary antibody was added and sections were incubated overnight at 4 degrees. The following day, sections were washed 4X in PBS, incubated with Donkey anti-Mouse 488 secondary antibody (Jackson Labs, 1:200) in PBS containing 1% BSA for 2 hours at room temperature, washed, mounted and coverslipped with Vectashield mounting medium containing DAPI.

Fos immunohistochemistry

For measurement of fos-like immunoreactivity in mouse CeA, animals were perfused 90-120 min after the first 10 min of the binge access period (Figures 2 and S1). On day 1 sections were washed, permeabilized in 50% methanol for 30 min, quenched in 3% hydrogen peroxide for 5 min, washed, and then blocked in PBS containing 0.3% Triton X-100 and 0.5% BSA for 1 hour. *c-fos* primary antibody (Santa Cruz Biotechnology - sc-52) was added to sections at 1:3000 and sections were incubated for 24-48 hours

at 4 degrees. On day 2, sections were washed in TNT buffer (0.1 M Tris-HCl pH 7.5, 0.15 M NaCl, 0.05% Tween-20) for 10 min, blocked in TNB buffer (0.1 M Tris-HCl pH 7.5, 0.15 M NaCl, 0.5% Blocking reagent – PerkinElmer FP1020) for 30 min. Sections were incubated in secondary antibody (Goat anti-rabbit HRP-conjugated- Sigma) 1:200 in TNB buffer for 30 min., washed in TNT buffer 4X for 5 min, and then incubated in Fluorescein diluted in TSA amplification diluents for 10 min. Sections were then washed 2X in TNT buffer, mounted, and coverslipped using Vectashield mounting medium containing DAPI.

Fluorescence in situ *hybridization (FISH)*

Pnoc-IRES-Cre or wild-type C57BL6/J mice were sectioned at 12 μM using standard cryosectioning and mounted directly to microscope slides (Fisherbrand Superfrost, cat no. 12-550-15). FISH was performed using the Affymetrix ViewRNA 2-plex assay according to the manufacturer's instructions. For assessment of *Cre/Pnoc* mRNA expression, we used a Type 1 Cre probe and a Type 6 *Pnoc* probe. For assessment of *Pnoc* with *Crh, Nts, Tac2, Calcr, Htr2a, Prkcd,* or *Sst*, we used RNAscope (Figure S2) (ACD - Newark, CA) according to the manufacturer's instructions.

Virus Injections and Survival Surgery

Following our first set of experiments, we did not observe any significant behavioral differences between Cre+ and Cre– littermates expressing viral transgenes. Therefore, Cre– littermates were used for all subsequent cohorts. *Pnoc-IRES*-Cre mice were anesthetized under isoflurane (0.5%–4%), and the skull surface exposed under sterile conditions. Using stereotaxic technique, 300 nL of virus was injected bilaterally into the CeA at 1.3 mm posterior of bregma, 2.9 mm lateral to the midline, and 4.60 mm ventral of bregma. Virus was injected at 100 nl/min (KD Scientific – model 100) directly using a Hamilton Syringe (7001) and allowed to diffuse for 5 min after injection before removing the needle. We injected cholera toxin B (CTB) at a volume of 200 nl. All viruses were generated by the UNC Vector Core Facility, aliquoted, and stored at −80 degrees.

CTB Tracer Injections for multiplexing with Pnoc and c-fos

Pnoc$^{\text{IRES-Cre}}$; L10-GFP mice were singly housed and injected bilaterally with CTB in the BNST, PBN, or NTS. After a recovery period of 5 days where all animals were exposed to HFD to prevent neophobia, animals were either given no food or 1 hour intermittent access to HFD. Chow was available *ad libitum* for both groups. Animals were transcardially perfused and the tissue processed for *c-fos* immunohistochemistry as described above. L10-GFP and CTB were imaged using epifluorescence.

In vivo *optogenetic surgeries*

Pnoc$^{\text{IRES-Cre}}$ mice were injected in the CeA as described above with 300 nL of AAV5-EF1α-DIO-ChR2(H134R)-eYFP and implanted bilaterally with chronic indwelling optical fibers (Sparta et al., 2011) in the parabrachial nucleus (PBN) at 5.45 mm posterior, +/− 1.37 lateral, and 3.55 ventral of bregma, in the nucleus of the solitary tract using a 10 degree angle at 6.90 posterior, +/− 1.50 lateral, and 4.75 mm ventral of bregma, and in the vBNST using a 10 degree angle at +0.2 posterior, +/− 1.05 lateral, and 4.70 ventral of bregma. For CeA optical fiber surgeries, we wedded the optical fiber to a small beveled needled (bias grind of 23 degrees) and implanted the optical fiber/needle using a 15-degree angle at −1.45 posterior, +/− 3.95 lateral, and 4.45 ventral of bregma. In this way, we minimized blue light stimulation of the adjacent BLA. For the NTS optical fibers, more rostral positions were used to so as to avoid damage of the Area Postrema and medial solitary tract nuclei that occur within a small 3-D space at ∼-7.4 mm posterior of bregma where many of the *Pnoc*$^{\text{CeA}}$ fibers terminate. Optical fibers were sealed in place using Zap-A-Gap glue and accelerant. A protective head cap was formed using black dental cement (Lang Dental). Animals were closely monitored and supplied with acetaminophen for 10 days following the surgery. We waited at least 6 weeks to allow for sufficient trafficking and expression of ChR2 at CeA, PBN, NTS, and vBNST axon terminals.

For *in vivo* optical tagging studies, mice were anesthetized with 2% Isoflurane (v/v) in oxygen (Baxter Healthcare, Deerfield, IL) during surgery. Mice received bilateral microinfusions of AAV5-EF1α-DIO-ChR2(H134R)-eYFP, infused at a rate of 100 nL/min and targeted at the CeA (1.3mm posterior, 2.8mm lateral, and 4.85mm ventral relative to Bregma). After each infusion, the syringe was left in place for 10 min to allow for diffusion. Mice were then implanted with bilateral chronic optical fibers targeted 0.1 mm dorsal to viral injection site and a unilateral electrode micro-array (Innovative Neurophysiology Inc, Durham, NC) targeted at the CeA (at 15 degrees anteroposterior, entry at: 0.33mm anterior, 2.75mm lateral, and 5.05mm ventral relative to Bregma). Mice were housed singly and allowed at least 3 weeks to recover prior to any behavioral testing.

iDISCO+ protocol

Sample processing

Mouse brains were cleared and immunolabeled following the procedures decribed by Renier et al. (2016). Samples were processed with the May 2016 version of the iDISCO+ protocol available at http://idisco.info. Briefly, n = 4 adult male *Pnoc*$^{\text{IRES-Cre}}$; *Ai9* reporter mice with deeply anesthetized and transcardially perfused with 30mL of PBS followed by 30mL of 4% PFA in PBS. Samples were post-fixed overnight at 4°C in 4% PFA in PBS and then stored in PBS at 4°C until use. Individual brains were hemisected and the hemisphere taken from each animal (left or right) was counterbalanced to include an equal number of hemispheres from each side. Brains then underwent sample pretreatment, permeabilization, and blocking as described in the protocol. Hemispheres were then incubated for 7 days at 37°C with shaking in 1:1000 Rabbit anti-RFP (Rockland Immunochemicals #600-401-379) recognizing tdTomato in the reporter mice. Samples then underwent 1 day of washing as described in the protocol and were incubated for

7 days at 37°C with shaking in 1:500 Donkey anti-Rabbit Alexa Fluor 647 (Thermo Fisher #A-31573). Samples then underwent one final wash followed by dehydration and tissue clearing as described in the protocol. Brains were stored in the dark at room temperature in Dibenzyl ether until they were imaged.

Light sheet imaging

Cleared samples were imaged in sagittal orientation (lateral side up) on a light-sheet microscope (Ultramicroscope II, LaVision Biotec) equipped with a sCMOS camera (Andor Neo) and a 2X/0.5 objective lens (MVPLAPO 2x) equipped with a 5.7 mm working distance dipping cap with correction optics. Versions v5.0.265-338 of the Inspector Microscope controller software was used. The microscope is equipped with LED lasers (488nm and 640nm) with 3 fixed light sheet generating lenses. The emission filters used were 525/50 and 680/30. For imaging in the 647 channel, a tiled grid of 7 × 5 was made with 2X zoom magnification (4X effective magnification) to cover the forebrain and cerebellum. Scans were performed with a light sheet numerical aperture of 0.034 and a z-step of 6 μm. The field of view was cropped to 1000 × 1000 pixels to reduce aberrations at the edges of the frame and stacks were acquired with a 10% overlap in X and Y. Tiled stacks were then converted to Imaris Files (Imaris Converter version 9.1.2) and stitched offline using the Imaris Stitcher (version 9.1.2). Imaging in the 488 channel was collected only for the purpose of alignment to the anatomical atlas, and was acquired at 0.8X zoom (1.6X effective magnification) as a single stack without tiling. The same sheet NA and z-step were used as the 647 channel. To speed up the acquisition, the two channels were acquired in separate scans. To account for possible movement of the sample between imaging in 488 and 647 channels, a 3D transformation was performed in ClearMap to align the two channels.

Image processing and analysis

Automated sample alignment and segmentation was performed using the ClearMap software developed by Renier et al. (2016). The scripts were implemented in Python 2.7 on a Dell Precision Tower 5810 running Ubuntu 16.04 LTS. The ClearMap software was installed from the August 2, 2016 release available on the GitHub repository (https://github.com/ChristophKirst/ClearMap) and image processing followed steps outlined in the tutorial. Briefly, the background was removed by subtraction with a disk shape structure element with a main axis of 7 pixels of diameter. Preliminary analysis of the segmentation results showed that spatial smoothing greatly improved the signal to noise ratio, and thus Difference of Gaussian (DoG) smoothing using a kernel of 8 × 8 x 4 voxels was applied to all images. Cells were detected from peaks with an intensity cutoff of 10. Watershed analysis was then performed to assess the size of the peak, and only detected features with sizes between 20 to 500 contiguous voxels were included as cells. The autofluorescence (488) and 647 channels were resampled to the same pixel size and underwent a 3D affine transformation to adjust for any movement between scans. The autofluorescence channel then underwent an automated registration to the Allen Brain Institute 25μm map, and companion annotation map (http://alleninstitute.org/). Together the transformation vectors were then applied to the results of the segmentation to compute cell counts for each region. To gain deeper insight into the distribution of *Pnoc* neurons within the CeA, the corresponding Numpy array for all points detected within the ROI was exported. Cell counts were binned in 100 μm intervals to assess the spread of nociception neurons along the anterior/posterior axis of the CeA. As a measure of quality control, hand drawn ROIs encompassing the CeA were drawn in Imaris to encompass the full anterior-posterior axis. Spot detection was then applied to the selected area and for each sample the counts for the CeA derived from the automatic segmentation were within ± 5% of counts derived from the manual annotation.

Feeding and Calorimetric Measurements

Calorimetry, activity, feeding, body composition & water intake measurements

Immediately prior to beginning and following the end of our experiments, we weighed the mice and measured body composition using magnetic resonance imaging (EchoMRI) to determine fat mass, lean mass, free water, and total water. For assessment of the effects of ablation *of* $Pnoc^{CeA}$ neurons on feeding, we used a comprehensive closed-loop calorimeter (TSE Systems) that allowed simultaneous assessment of activity (beam breaks), oxygen utilization (VO2) and carbon dioxide production (VCO2), respiratory exchange, water intake, and food intake (Figure S3). In part to allow for acclimation to these new cages, mice were given *ad libitum* access to standard rodent chow for 7 days. On the 8^{th} day, we continued *ad libitum* access to standard rodent chow, but added a second food hopper containing *ad libitum* HFD for one hour (11 am – 4 hours into the light cycle). In this way, we induced hyperphagia of HFD without interrupting other measurements. This schedule of intermittent access was continued for 4 complete days or 5 total binge cycles. On the last binge cycle the HFD was not removed and chow diet was removed to shift them to a continuous HFD schedule for 3 days.

In a separate experiment, mice were returned to their home cages and placed back on *ad libitum* chow for one week. To assess the effects of $Pnoc^{CeA}$ ablation on basal metabolic rate, chow was removed from the animal's cage at lights on (7 AM), animals were placed in the calorimeters, and VO2 and VCO2 assessed over a period of 7 hours.

Core body temperature measurement

Animals were briefly and lightly anesthetized using isoflurane and rectal temperature was measured using a Physitemp Thermalert TH-5 and a RET-3 rectal probe. We observed stable temperatures after 20-30 s. Measurements were performed at 9:00 AM (2 hours into light cycle) and 9:00 PM (2 hours into dark cycle).

Assessment of Pnoc^{CeA} effect on Diet-Induced Obesity

In a completely separate cohort of FLEX-Caspase or control injected animals, we measured body weights and overnight food intake in their home cages during 5 weeks of access to chow, one week of intermittent access to HFD, and 9 weeks of HFD. This schedule matched our acute schedule but increased HFD access from 3 days to 9 weeks.

Assessment of Pnoc^{CeA} effect on 2- bottle choice preference for positive and negative valence tastants

In a completely separate cohort of FLEX-Caspase or control injected animals, we individually housed animals in cages with access to two water bottles. In a counterbalanced fashion, mice were exposed to increasing concentrations of quinine or saccharin with 4 days of washout between different tastants. Mice and bottles were weighed every 24 hours 8 hours into the light cycle.

In vivo electrophysiology and optical tagging of Pnoc^{CeA} neurons

Behavioral testing

Mice were food deprived overnight prior to *in vivo* electrophysiology experiments. Recording sessions took place in the homecage, and consisted of an initial phototagging period, during which 10x 5 s trains of blue light pulses (450nm at 20 Hz; 10 s ITI) were delivered to the CeA via the implanted optic fibers. Any neuron exhibiting significantly increased firing rate (< 5 ms latency) in response to the laser pulses was considered to be *Pnoc*+. All other neurons were classified as non-*Pnoc*.

Immediately following the phototagging test, mice were allowed to move freely in their cage for 10 min during a Laser-OFF period that would serve as the baseline for behavior and neural activity. After baseline, mice were presented with quinine-adulterated chow, unadulterated chow, and a novel high fat (i.e., ''palatable'') food, each during 16-min intervals consisting of 4x 2-min Laser OFF + 2-min Laser ON blocks (counterbalanced across mice). This allowed us to record neural activity during eating bouts and to observe whether eating was affected by laser stimulation for each food type. It should be noted that the order of food was always quinine-adulterated chow, non-adulterated chow, then palatable food, as the mice would not consume the adulterated chow if they were given time to eat the non-adulterated or palatable foods first. Only the neurons of animals that consumed all three foods were kept in the analysis.

Electrophysiological recording and single unit analysis

Individual units were identified and recorded using Omniplex Neural Data Acquisition System (Plexon Inc, Dallas, TX). Neural data was sorted manually using Offline Sorter (Plexon Inc, Dallas, TX). To be included in the analyses, units had to exhibit a refractory period of at least 1 ms. Autocorrelograms from simultaneously recorded units were examined to ensure that no cell was counted twice. Individual t tests for food type were run to determine whether each cell type (*Pnoc* versus non-*Pnoc*) significantly changed firing rate during eating bouts. Data reported for raw firing rates include only putative principal neurons (< 10Hz).

Slice Electrophysiology

Pnoc$^{fRES\text{-}Cre}$ mice with a AAV8-hSyn-DIO-hM4D-mCherry or AAV5-EF1a-DIO-ChR2-eYFP virus injected into the CeA were decapitated following deep isoflurane anesthesia, then brains were extracted and placed in ice-cold sucrose artificial cerebrospinal fluid (aCSF) containing (in mM) 194 sucrose, 20 NaCl, 4.4 KCl, 2 $CaCl_2$, 1 $MgCl_2$, 1.2 NaH_2PO_4, 10.0 glucose, and 26.0 $NaHCO_3$ saturated with 95% O_2/5% CO_2. Brains from *Pnoc*-GFP mice were extracted following transcardial perfusion with NMDG ACSF (see below). For sucrose aCSF, coronal sections of the CeA were sliced at 300 μm on a Leica 1200S vibratome at 0.07 (mm/s). Slices were incubated in a heated holding chamber containing normal, oxygenated aCSF [(in mM): 124 NaCl, 4.4 KCl, 2 $CaCl_2$, 1.2 $MgSO_4$, 1 NaH_2PO_4, 10.0 glucose, and 26.0 $NaHCO_3$] maintained at 30 ± 1°C for at least 1 hour before recording. Slices were then transferred to a recording chamber (Warner Instruments), submerged in normal, oxygenated aCSF (containing 0.5 μM TTX for hM4D experiments) and maintained at 28-30°C with a flow rate of 2 ml/min. CeA neurons were visualized using infrared differential interference contrast (DIC) video-enhanced microscopy (Olympus) and DREADD-expressing cells were identified by mCherry fluorescence. Whole-cell patch clamp recordings were made in current clamp mode with a potassium gluconate-based intracellular solution (in mM: 135 K-gluconate, 5 NaCl, 2 MgCl2, 10 HEPES, 0.6 EGTA, 4 Na2ATP, 0.4 Na2GTP, pH 7.3, 285–290mOsmol). After achieving a stable baseline for 4 minutes, 10 μM CNO was applied to the bath for 10 minutes. Signals were digitized at 10 kHz and filtered at 3 kHz using a Multiclamp 700B amplifier, then analyzed using Clampfit 10.3 software (Molecular Devices, Sunnyvale, CA). For a subset of ChR2-injected animals, terminally anesthetized animals were transcardially perfused with a low Na^+ aCSF containing in mM 93 N-methyl-D-glucamine, 2.5 KCl, 1.2 NaH_2PO_4, 30 $NaHCO_3$, 20 HEPES, 25 Glucose, 5 L-ascorbic acid, 2 Thiourea, 3 sodium pyruvate, 10 $MgSO_4 \cdot 7H_2O$, 0.5 $CaCl_2X2H_2O$. After slicing, 250 μm slices were placed in 32°C NMDG aCSF for no more than 8 minutes and then transferred to normal oxygenated aCSF (see below). We observed that this process of NMDG perfusion and recovery greatly improved hindbrain health and cell visibility. To validate ChR2 function in *Pnoc*^{CeA} cells, we identified ChR2-expressing cells under brief blue light illumination and then recorded light evoked changes in action potentials in current clamp mode across a range of stimulation frequencies. To assess functional connectivity in downstream regions, we patched cells in fields of the vBNST, PBN, and NTS containing dense ChR2 fibers in aCSF containing 3 mM kynurenic acid to isolate putative evoked inhibitory postsynaptic currents. In a subset of slices, we also included 0.5 μM TTX and 100 μM 4-AP to isolate monosynaptic responses. Each cell was run through a paired-pulse protocol containing a baseline period and two 5 ms blue light pulses. Average responses were determined following 10 sweeps.

Chemogenetic and Optogenetic Behaviors

For all behavioral experiments, mice were moved from the vivarium to the behavioral facility and allowed to acclimate in a holding area for at least 30 minutes prior to the start of the 1st assay. Blue light was supplied using a fiber-coupled laser through a fiber optic rotary joint and bilateral patch cable (Doric). Laser output was adjusted to 12 mW for each end of the patch cable. Laser light was pulsed at a constant frequency of 1, 10, 20, or 40 Hz using a TTL-pulse driven Arduino. Behavior was recorded and lasers driven using Ethovision or MedPC IV.

Chemogenetic feeding experiments

DREADD feeding experiments were performed in the animal's home cage in the vivarium. Each day at 10 AM (3 hours into the light cycle) animals were weighed and their home cage intake of chow measured, after which the chow was removed. Each mouse was injected with 3 mg/kg clozapine N-oxide (CNO). 30 min later food was added to the cage and its weight measured every hour for 3 hours (food access start at 11 AM). Fresh chow was added and its weight recorded after the last measurement except in cases of food deprivation. In this way, we were able to measure both DREADD-mediated and home cage food consumption throughout the experimental timeline. CNO injections and exposure to highly palatable foods was performed every other day to avoid feeding entrainment that results in a significant reduction in home cage intake.

Chemogenetic liquid tastant intake

Experiments were performed 3-4 hours into the light cycle. In some cases, we water deprived animals for 24 hours to generate a motivated state for liquid consumption (Figure S4). Animals were injected with CNO or vehicle 30 minutes prior to access to bottles containing water, 1.0 mM quinine, or grape kool-aid (0.05% w/v containing 0.15% saccharin). Solutions were made up fresh on the day of the assay.

Optogenetic Feeding Assays

Because of the modulation of feeding behavior by metabolic state, environment, and food palatability, we assessed consumption of both normal mouse chow and high-fat food in both the mouse's home cage (Figure S5). In each of these 20 min sessions, we stimulated the vBNST, PBN, and NTS pathways at 40 Hz. For cell body stimulation, we stimulated at 5 Hz.

Novelty Induced Suppression of Feeding

Mice were preexposed to fruit loops in their home cage at least twice prior to the assay day. On the day before the assay, mice were food deprived. On the assay day, animals were moved and allowed to habituate to the behavioral facility for 45 minutes. 30-45 min prior to their assay they were injected with 3 mg/kg CNO. Each animal was placed in a large rat cage with fresh bedding containing a fruit loop placed on a 7 cm disk of filter paper in its center. The entire behavioral arena was recorded using Media Recorder connected to a PC computer running Windows 7. The latency to feed on the fruit loop was measured by hand, and, upon obvious feeding, the animal was moved back into its homecage and allowed to feed on a preweighed amount of fruit loops for 10 minutes after which the fruit loops were removed and weighed.

For optogenetic experiments, mice were preexposed to fruit loops in their home cage twice and food deprived the night before the assay. On the day of the assay, mice attached to patch cables were placed in a novel environment (rat cage) with a single fruit loop while providing 40 Hz stimulation (Figure S5). After the first consummatory bout, the fruit loop was removed and stimulation was continued until 10 min of stimulation had elapsed in the novel environment. Mice were then transferred to their home cage and allowed access to *ad libitum* fruit loops for 10 min while continuing 40 Hz stimulation. We used 5 Hz for stimulation of $Pnoc^{CeA}$ cell bodies.

Open Field Assay

Mice were placed in a square white Plexiglas arena measuring 20.5 in. on each side and their movement recorded using a CCD camera (Figure S5). Mice were allowed to explore the box for 20 min. Behavior was tracked using Ethovision XT (Noldus Information Technology), where center was defined as the middle half of the box in both the X and Y planes.

For optogenetic experiments, since we observed a highly significant place preference using a 40 Hz frequency, we used this frequency to assess anxiety-like behavior in vBNST, PBN, and NTS cohorts. We used 5 Hz for stimulation of $Pnoc^{CeA}$ cell bodies. Mice were attached to patch cables and placed in a square white Plexiglas arena measuring 20.5 in. on each side and their movement recorded using a CCD camera. Mice were allowed to explore the box for 18 min providing laser stimulation for alternating 3 min intervals OFF-ON-OFF-ON-OFF-ON. For the NTS cohort, videos for one Cre+ and one Cre- mice were corrupted and unable to be tracked.

Elevated Plus/Zero Maze

Mice were placed in an elevated plus maze (two 30 inch arms, one close and one open) or elevated zero maze (24 inch diameter with alternating open and closed quandrants) and allowed to explore the open and closed arms for 5 minutes (Figure S5). Exploratory behavior was tracked as previously described in the open field section.

For optogenetic experiments, mice were placed in a standard design elevated plus maze and allowed to explore the open and closed arms for 10 minutes: the first 5 min with 40 Hz blue laser stimulation and the second 5 min with no stimulation. We used 5 Hz for stimulation of $Pnoc^{CeA}$ cell bodies.

Light/Dark Box Conflict Assay

Mice were placed in a two-sided chamber containing a dark enclosed side and a brightly lit open side and allowed to explore both sides for 15 min. Behavior was tracked as previously described in the open field section (Figure S4).

Real Time Place Preference

For assessment of optogenetic real time place preference, animals were attached to patch cables and placed in a two-sided chamber where one side was paired with laser stimulation and allowed to explore for 20 min. Laser-paired sides were alternated and counterbalanced for each animal across experimental days using different stimulation frequencies.

Optogenetic Self-Stimulation

For optogenetic self-stimulation experiments, mice were food restricted for a period beginning two days before the first behavioral test day. Mice were weighed daily and given access to < 3 g of chow each night. Bodyweights were never allowed to drop below 85% of their starting weight.

Operant boxes were outfitted with two nose poke ports and a cue light. Prior to each session, both nose poke ports were baited with 3-4 mg of chow. Mice were attached to patch cables and allowed to explore the box and the ports for 30 min. During this session, each nose poke of the active port triggered 5 s of laser stimulation (either 10 or 40 Hz – 10 Hz data in Figure S5) and concomitant activation of the cue light. Within the Cre – and Cre + groups, we counterbalanced the active port position (left or right) and the order of either 10 Hz or 40 Hz on separate experimental days. Following these two frequencies, we assayed nose poking during a ''laser off'' session on a separate day.

QUANTIFICATION AND STATISTICAL ANALYSIS

Statistical parameters like n and the specific tests performed can be found in the figure legends. Statistical analyses were performed in Prism 6.0h (Graphpad, La Jolla, CA). For determination of statistical significance, we used an alpha of 0.05. Error bars represent ± SEM.